

# Broadband Study of Gamma-Ray Blazars at Redshifts $z = 2.0 - 2.5$

N. Sahakyan<sup>1</sup>, <sup>\*</sup> G. Harutyunyan<sup>1</sup>, S. Gasparyan<sup>1</sup>, D. Israyelyan<sup>1</sup>

<sup>1</sup>ICRANet-Armenia, Marshall Baghramian Avenue 24a, Yerevan 0019, Armenia

Accepted XXX. Received YYY; in original form ZZZ

## ABSTRACT

High redshift blazars are among the most powerful non-explosive sources in the Universe and play a crucial role in understanding the evolution of relativistic jets. To understand these bright objects, we performed a detailed investigation of the multiwavelength properties of 79  $\gamma$ -ray blazars with redshifts ranging from  $z = 2.0$  to  $2.5$ , using data from Fermi LAT, Swift XRT/UVOT, and NuSTAR observations. In the  $\gamma$ -ray band, the spectral analysis revealed a wide range of flux and photon indices, from  $5.32 \times 10^{-10}$  to  $3.40 \times 10^{-7}$  photons  $\text{cm}^{-2} \text{s}^{-1}$  and from 1.66 to 3.15, respectively, highlighting the diverse nature of these sources. The detailed temporal analysis showed that flaring activities were observed in 31 sources. Sources such as 4C+71.07, PKS 1329-049, and 4C+01.02, demonstrated significant increase in the  $\gamma$ -ray luminosity and flux variations, reaching peak luminosity exceeding  $10^{50}$  erg  $\text{s}^{-1}$ . The temporal analysis extended to X-ray and optical/UV bands, showed clear flux changes in some sources in different observations. The time-averaged properties of high redshift blazars were derived through modeling the spectral energy distributions with a one-zone leptonic scenario, assuming the emission region is within the broad-line region (BLR) and the X-ray and  $\gamma$ -ray emissions are due to inverse Compton scattering of synchrotron and BLR-reflected photons. This modeling allowed us to constrain the emitting particle distribution, estimate the magnetic field inside the jet, and evaluate the jet luminosity, which is discussed in comparison with the disk luminosity derived from fitting the excess in the UV band.

**Key words:** galaxies: active – radiation mechanisms: non-thermal – X-rays: galaxies – gamma-rays: galaxies

## 1 INTRODUCTION

Blazars are jetted active galactic nuclei (AGN) and are among the most powerful persistent sources of electromagnetic radiation in the universe. Current unification theories assumes that blazars are a subtype of AGNs with jets oriented at a small angle relative to the observer’s line of sight (Urry & Padovani 1995). Their emission is believed to be primarily powered by the accretion of matter into supermassive black holes (Blandford & Znajek 1977) and exhibit extreme characteristics, such as high-amplitude and short-timescale variability, core dominance, superluminal motion, and significant optical polarization. Blazars are typically grouped into two main groups based on the presence of emission lines in their spectra (Urry & Padovani 1995): BL Lacertae objects (BL Lacs), which have weak or absent emission lines, and flat spectrum radio quasars (FSRQs), which display strong emission lines.

The nonthermal emission from the jets of blazars is observable across almost all accessible bands of the electromagnetic spectrum (Padovani et al. 2017) up to high energy (HE;  $> 100$  MeV) and (VHE;  $> 100$  MeV)  $\gamma$ -ray bands. Their broadband spectral energy distribution typically shows two broad humps. The lower-energy component, from the radio to the optical/X-ray band, is generally attributed to the synchrotron emission of electrons. The frequency of the synchrotron peak ( $\nu_p$ ) serves as a criterion to further classify blazars: as low synchrotron peaked sources (LSPs or LBLs), intermediate synchrotron peaked sources (ISPs or IBLs), or high synchrotron peaked sources (HSPs or HBLs) when  $\nu_p < 10^{14}$  Hz,  $10^{14}$  Hz  $< \nu_p < 10^{15}$  Hz, and

$\nu_p > 10^{15}$  Hz, respectively (Padovani & Giommi 1995; Abdo et al. 2010). The origin of the second component, however, remains a subject of debate. In leptonic scenarios, this second peak is interpreted as the result of inverse Compton scattering of low-energy photons, which may be of internal or external origin. In the synchrotron self-Compton (SSC) models (Ghisellini et al. 1985; Maraschi et al. 1992; Bloom & Marscher 1996), it is the synchrotron photons that are up-scattered through inverse Compton processes. On the other hand, external inverse Compton (EIC) scenarios (e.g., Sikora et al. 1994) suggest that the photons originate outside the jet, coming directly from the accretion disk (Dermer et al. 1992; Dermer & Schlickeiser 1994), or they may be reprocessed by the broad-line region (BLR) (Sikora et al. 1994), or emitted from the torus (Błażejowski et al. 2000). In Bégué et al. (2023), a novel approach for fitting the blazar Spectral Energy Distribution (SED) utilizing convolutional neural networks is introduced which allows self-consistent modeling, enabling a more detailed interpretation of the observed results.

In alternative models such as the hadronic or lepto-hadronic scenarios, the second spectral bump is assumed to be from the synchrotron emission of ultra-HE protons or from the decay of secondary particles produced during hadronic interactions (Mannheim 1993; Mannheim & Biermann 1989; Mücke & Protheroe 2001; Mücke et al. 2003; Böttcher et al. 2013; Petropoulou & Mastichiadis 2015; Gasparyan et al. 2022). Interest in these models has increased, particularly after establishing a potential link between blazars and VHE neutrinos, following the association of TXS 0506+056 with the IceCube-170922A neutrino event (IceCube Collaboration et al. 2018a,b; Padovani et al. 2018), and the detection of multiple neutrino events concurrent with the active phase of PKS 0735+178 in

\* E-mail: narek@icra.it

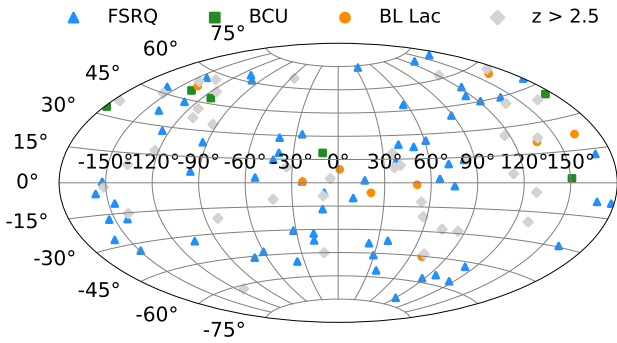


**Figure 1.** Hammer-Aitoff projection in Galactic coordinates showing the distribution of  $\gamma$ -ray blazars with redshifts above  $z > 2.0$ . BL Lacs within the redshift range  $2.0 \leq z \leq 2.5$  are represented by orange symbols, FSRQs are depicted in blue, BCUs in green, and blazars with redshifts  $z > 2.5$  are shown as grey diamonds.

optical/UV, X-ray, and  $\gamma$ -ray bands (Sahakyan et al. 2023a). These multimessenger observations have started extensive discussions, with various models being applied to explain the multimessenger observations of blazars (Ansoldi et al. 2018; Keivani et al. 2018; Murase et al. 2018; Padovani et al. 2018; Sahakyan 2018; Righi et al. 2019; Cerruti et al. 2019; Sahakyan 2019; Gao et al. 2019; Gasparyan et al. 2022).

The emission from blazars is highly beamed, and their bolometric luminosity can exceed  $10^{48} \text{ erg s}^{-1}$ , allowing them to be observed even at very high redshifts (e.g., see Ackermann et al. 2017; Sahakyan et al. 2020). These distant blazars are particularly interesting, as their study offers insights into the formation and evolution of supermassive black holes, relativistic jets, and the connections between accretion disks and jets. Moreover, their  $\gamma$ -ray emission is important for probing the early universe;  $\gamma$ -ray emission from distant blazars undergoes attenuation via  $\gamma\gamma$  absorption when interacting with extragalactic background light (EBL) photons, thereby enabling observations that can constrain the EBL’s density. The multiwavelength properties of distant blazars have been extensively studied in a number of publications (e.g., see Sahakyan et al. 2023b, 2020; Li et al. 2020; Liao et al. 2019; Marcotulli et al. 2017; Orienti et al. 2016; D’Ammando & Orienti 2016; Paliya et al. 2015; Pacciani et al. 2012; Paliya 2015; Paliya et al. 2016, 2017, 2019). In Sahakyan et al. (2020), the origin of emission from the most distant blazars detected in the HE  $\gamma$ -ray band ( $z > 2.5$ ) was investigated analyzing data in the optical/UV, X-ray, and  $\gamma$ -ray bands. From the temporal evolution of emission in these bands, flaring periods were identified when the luminosity substantially increased. Their broadband emission was modeled using one-zone SSC and EIC models, assuming that the external photons are infrared (IR) photons from the dusty torus (see Arsioli & Chang (2018) for a discussion on the contribution of different external fields in shaping the HE emission of LSPs). As a result, the parameters that characterize the particle emission and jet in these distant blazars were estimated.

In this work, we expand the study by Sahakyan et al. (2020) to  $\gamma$ -ray emitting blazars which have estimated redshifts that are in the range of  $z = 2.0 - 2.5$ . A prolonged observation period of  $\sim 14$  years enables a comprehensive investigation of emissions from these sources across optical/UV, X-ray, and  $\gamma$ -ray bands as well as to perform detailed spectral and temporal analysis. Using the analyzed data broadband SEDs for a substantial number of sources were constrained and modeled which allows for a systematic comparison of

blazar emission parameters at varying distances, which, in turn, could enhance our understanding of these brightest objects.

The structure of the paper is as follows: Section 2 introduces the sample of sources under consideration; Section 3 details the data analysis methodology; Section 4 presents the results of the data analysis; Section 5 discusses the modeling of broadband SEDs; and Section 6 outlines the modeling results. Finally, the conclusions are summarized in Section 7.

## 2 SOURCE SAMPLE

The fourth catalogue of AGNs detected by the Fermi Large Area Telescope (*Fermi*-LAT) (Ajello et al. 2022) contains 3,814 blazars, among which 792 are FSRQs, 1,458 are BL Lacs, and 1,493 are BCUs. The most distant blazar, GB 1508+5714, is at  $z = 4.31$ . A small fraction of the blazars, 79 (2.07%), have a redshift between  $2.0 < z < 2.5$ , and these are the ones selected for the current study (the source sample). This group includes 64 FSRQs, 9 BL Lacs, and 6 BCUs. The BL Lacs generally have redshifts lower than  $z = 2.1$ , with the exception of SDSS J145059.99+520111.7, which is at  $z = 2.47$ . Among the BL Lacs, there are 3 LBLs, 4 IBLs, and only 2 HBLs. The FSRQs have a more homogeneous redshift distribution, being observed at almost all redshifts; the most distant FSRQ in the sample is S5 1053+70 at  $z = 2.49$ . BCUs, which exhibit characteristics similar to blazars but lack reliable optical associations, have been observed across a range of redshifts. For instance, 4FGL J1139.0+4033 (CRATES J113903+403303) has been observed at  $z = 2.36$ , while 4FGL J1003.4+0205 (SDSS J100326.63+020455.6) is located at  $z = 2.08$ . In Sahakyan et al. (2022a) BCUs were classified by training machine learning algorithms on the  $\gamma$ -ray properties of FSRQs and BL Lacs. According to those criteria, four BCUs from our sample show probability similar to FSRQs (CRATES J113903+403303, MG4 J162750+4802, TXS 2315+189 and SDSS J120542.82+332146.9), one to BL Lacs (SDSS J100326.63+020455.6) and one (SDSS J120542.82+332146.9) can not be classified.

In summary, the source sample considered in this study comprises 79 objects. In Table 1, the three leftmost columns list these sources along with their 4FGL names and classes. The spatial distribution of these blazars in Galactic coordinates is depicted in the Hammer–Aitoff projection shown in Fig. 1. For completeness, this figure also includes blazars with redshifts greater than  $z > 2.5$ , as reported by Sahakyan et al. (2020).

## 3 MULTIWAVELENGTH OBSERVATIONS OF CONSIDERED BLAZARS

In order to investigate the multiwavelength properties of the selected sources, data collected by the *Fermi*-LAT, Nuclear Spectroscopic Telescope Array (NuSTAR), Neil Gehrels Swift Observatory (hereafter Swift) X-Ray Telescope (XRT), and Ultraviolet/Optical Telescope (Swift UVOT) were downloaded and analyzed.

### 3.1 *Fermi*-LAT data

The Large Area Telescope (LAT), onboard the Fermi Gamma-ray Space Telescope, is a HE instrument that uses the pair-production technique to detect  $\gamma$ -rays in the energy range between 20 MeV and  $> 300$  GeV. By default, it operates in scanning mode, continuously

**Table 1.** The table shows the source sample, detailing the outcomes of the  $\gamma$ -ray analysis. For each source, the name, associated 4FGL name, and class are provided.  $\alpha_p$  represents the photon index when the source spectrum is best modeled with a power-law model, whereas  $\alpha$  and  $\beta$  denote the slope and curvature, respectively, when the spectrum is modeled with a log-parabola. The flux is reported in units of  $10^{-8}$  photons  $\text{cm}^{-2} \text{s}^{-1}$ , and the luminosity is expressed in  $10^{47}$  ergs  $\text{s}^{-1}$ . The redshift  $z$  is given in last column.

Object	4FGL name	Class	$\alpha_p/\alpha$	$\beta$	Flux	Luminosity	$z$
S5 1053+70	4FGL J1056.8+7012	FSRQ	$2.70 \pm 0.08$	$0.23 \pm 0.08$	$1.92 \pm 0.55$	$6.51 \pm 0.46$	2.492
PMN J1344-1723	4FGL J1344.2-1723	FSRQ	$2.03 \pm 0.04$	$0.14 \pm 0.02$	$1.68 \pm 0.14$	$9.79 \pm 0.5$	2.490
SDSS J145059.99+520111.7	4FGL J1450.8+5201	BLL	$2.11 \pm 0.08$	$0.09 \pm 0.04$	$0.64 \pm 0.16$	$3.79 \pm 0.44$	2.471
PKS 1915-458	4FGL J1919.4-4550	FSRQ	$3.15 \pm 0.12$	-	$1.47 \pm 0.18$	$2.19 \pm 0.26$	2.470
PKS 0226-559	4FGL J0228.3-5547	FSRQ	$2.24 \pm 0.02$	$0.11 \pm 0.01$	$5.04 \pm 0.18$	$22.1 \pm 0.49$	2.464
S3 2214+30	4FGL J2216.8+3103	FSRQ	$2.66 \pm 0.28$	$0.33 \pm 0.19$	$0.26 \pm 0.12$	$0.89 \pm 0.28$	2.462
PKS 2315-172	4FGL J2318.6-1657	FSRQ	$2.21 \pm 0.01$	-	$0.20 \pm 0.00$	$0.76 \pm 0.02$	2.462
PKS 0601-70	4FGL J0601.1-7035	FSRQ	$2.27 \pm 0.03$	$0.09 \pm 0.02$	$3.51 \pm 0.17$	$11.22 \pm 0.39$	2.409
B2 1436+37B	4FGL J1438.9+3710	FSRQ	$2.33 \pm 0.05$	$0.10 \pm 0.03$	$1.88 \pm 0.14$	$5.24 \pm 0.27$	2.401
2MASS J16561677-3302127 <sup>1</sup>	4FGL J1656.3-3301	FSRQ	$2.94 \pm 0.11$	$0.32 \pm 0.09$	$3.47 \pm 0.72$	$6.68 \pm 0.70$	2.400
MG1 J173624+0632	4FGL J1736.6+0628	FSRQ	$2.67 \pm 0.08$	-	$1.58 \pm 0.21$	$2.90 \pm 0.39$	2.387
TXS 1645+635	4FGL J1645.6+6329	FSRQ	$2.46 \pm 0.06$	$0.13 \pm 0.04$	$1.41 \pm 0.12$	$3.28 \pm 0.2$	2.379
PKS B1149-084	4FGL J1152.3-0839	FSRQ	$2.33 \pm 0.04$	$0.11 \pm 0.02$	$2.79 \pm 0.19$	$7.9 \pm 0.38$	2.370
S5 0212+73	4FGL J0217.4+7352	FSRQ	$2.93 \pm 0.04$	$0.15 \pm 0.03$	$3.52 \pm 0.17$	$5.56 \pm 0.2$	2.367
B2 0552+39A	4FGL J0555.6+3947	FSRQ	$2.67 \pm 0.00$	$0.15 \pm 0.00$	$3.98 \pm 0.02$	$7.5 \pm 0.02$	2.365
CRATES J113903+403303	4FGL J1139.0+4033	BCU	$2.73 \pm 0.09$	-	$1.13 \pm 0.18$	$1.90 \pm 0.30$	2.360
B2 2112+28B	4FGL J2114.8+2831	FSRQ	$2.50 \pm 0.21$	$0.42 \pm 0.18$	$0.33 \pm 0.15$	$1.54 \pm 0.36$	2.345
PKS 2149-306	4FGL J2151.8-3027	FSRQ	$2.86 \pm 0.03$	$0.17 \pm 0.03$	$7.01 \pm 0.21$	$10.85 \pm 0.3$	2.345
PKS 1430-178	4FGL J1433.0-1801	FSRQ	$2.71 \pm 0.02$	$0.30 \pm 0.01$	$0.60 \pm 0.03$	$1.53 \pm 0.1$	2.331
MG4 J162750+4802	4FGL J1627.3+4758	BCU	$2.64 \pm 0.16$	$0.11 \pm 0.11$	$0.46 \pm 0.16$	$0.96 \pm 0.21$	2.326
PMN J0743-5619	4FGL J0743.0-5622	FSRQ	$2.90 \pm 0.19$	-	$1.01 \pm 0.22$	$1.45 \pm 0.32$	2.319
GB6 J0742+4900	4FGL J0742.1+4902	FSRQ	$2.24 \pm 0.09$	-	$0.46 \pm 0.10$	$1.38 \pm 0.30$	2.312
S3 0458-02	4FGL J0501.2-0158	FSRQ	$2.29 \pm 0.01$	$0.09 \pm 0.01$	$10.80 \pm 0.19$	$27.57 \pm 0.4$	2.291
PMN J0157-4614	4FGL J0157.7-4614	FSRQ	$2.26 \pm 0.13$	$0.26 \pm 0.09$	$0.55 \pm 0.15$	$2.08 \pm 0.24$	2.287
PKS 0726-476	4FGL J0728.0-4740	FSRQ	$2.36 \pm 0.24$	-	$0.45 \pm 0.32$	$1.06 \pm 0.75$	2.282
PKS 0420+022	4FGL J0422.8+0225	FSRQ	$2.63 \pm 0.19$	$0.37 \pm 0.17$	$1.11 \pm 0.24$	$1.95 \pm 0.28$	2.277
PKS 2245-328	4FGL J2248.7-3235	FSRQ	$2.67 \pm 0.05$	-	$2.01 \pm 0.14$	$3.23 \pm 0.22$	2.268
PKS B2224+006	4FGL J2226.8+0051	FSRQ	$2.98 \pm 0.24$	$0.31 \pm 0.10$	$0.92 \pm 0.17$	$1.81 \pm 0.32$	2.262
TXS 1322+479	4FGL J1324.9+4748	FSRQ	$2.67 \pm 0.07$	-	$1.09 \pm 0.13$	$1.74 \pm 0.21$	2.260
PKS 2244-37	4FGL J2247.5-3700	FSRQ	$2.40 \pm 0.20$	-	$0.19 \pm 0.09$	$0.41 \pm 0.19$	2.252
B2 0242+23	4FGL J0245.4+2408	FSRQ	$2.67 \pm 0.05$	-	$1.98 \pm 0.16$	$3.09 \pm 0.25$	2.243
4C +71.07	4FGL J0841.3+7053	FSRQ	$2.81 \pm 0.02$	$0.21 \pm 0.02$	$10.68 \pm 0.17$	$14.76 \pm 0.23$	2.218
PKS 2022+031	4FGL J2025.2+0317	FSRQ	$2.07 \pm 0.06$	$0.09 \pm 0.03$	$0.92 \pm 0.13$	$4.03 \pm 0.37$	2.210
MG2 J174753+2323	4FGL J1747.4+2330	FSRQ	$2.79 \pm 0.03$	$0.39 \pm 0.03$	$0.80 \pm 0.03$	$1.2 \pm 0.03$	2.203
MG2 J153938+2744	4FGL J1539.6+2743	FSRQ	$2.23 \pm 0.06$	$0.05 \pm 0.03$	$1.18 \pm 0.13$	$3.12 \pm 0.23$	2.196
S4 0917+44	4FGL J0920.9+4441	FSRQ	$2.35 \pm 0.02$	$0.15 \pm 0.02$	$5.88 \pm 0.35$	$17.97 \pm 0.43$	2.186
PMN J2135-5006	4FGL J2135.3-5006	FSRQ	$2.40 \pm 0.05$	$0.10 \pm 0.03$	$1.99 \pm 0.13$	$3.92 \pm 0.2$	2.181
OX 131	4FGL J2121.0+1901	FSRQ	$2.14 \pm 0.03$	$0.05 \pm 0.01$	$2.68 \pm 0.17$	$8.77 \pm 0.38$	2.180
PMN J1959-4246	4FGL J1959.1-4247	FSRQ	$2.16 \pm 0.10$	$0.19 \pm 0.06$	$0.88 \pm 0.15$	$2.76 \pm 0.26$	2.174
B3 1520+437	4FGL J1521.8+4338	FSRQ	$3.00 \pm 0.10$	-	$1.14 \pm 0.15$	$1.32 \pm 0.17$	2.168
TXS 2315+189	4FGL J2318.2+1915	BCU	$2.60 \pm 0.01$	-	$1.60 \pm 0.03$	$2.43 \pm 0.05$	2.163
PKS 0446+11	4FGL J0449.1+1121	FSRQ	$2.37 \pm 0.03$	$0.13 \pm 0.02$	$6.25 \pm 0.21$	$12.12 \pm 0.34$	2.153
PKS 1329-049	4FGL J1332.0-0509	FSRQ	$2.41 \pm 0.02$	$0.16 \pm 0.02$	$6.33 \pm 0.18$	$11.57 \pm 0.32$	2.150
PMN J2227+0037	4FGL J2227.9+0036	BLL	$1.77 \pm 0.11$	$0.15 \pm 0.05$	$0.31 \pm 0.10$	$3.79 \pm 0.54$	2.145
TXS 2321-065	4FGL J2323.6-0617	FSRQ	$2.32 \pm 0.10$	$0.18 \pm 0.06$	$0.87 \pm 0.16$	$2.14 \pm 0.24$	2.144
PMN J1402-3334	4FGL J1402.6-3330	FSRQ	$3.08 \pm 0.28$	$1.30 \pm 0.37$	$0.61 \pm 0.13$	$1.44 \pm 0.21$	2.140
PMN J0134-3843	4FGL J0134.3-3842	FSRQ	$2.59 \pm 0.08$	-	$0.72 \pm 0.10$	$1.07 \pm 0.15$	2.140
87GB 080551.6+535010	4FGL J0809.5+5341	FSRQ	$2.19 \pm 0.04$	$0.10 \pm 0.02$	$1.71 \pm 0.14$	$5.03 \pm 0.26$	2.133
87GB 142651.1+564919	4FGL J1428.3+5635	FSRQ	$2.69 \pm 0.03$	-	$0.44 \pm 0.03$	$0.60 \pm 0.04$	2.129
PKS B1043-291	4FGL J1045.8-2928	FSRQ	$2.61 \pm 0.07$	-	$1.24 \pm 0.15$	$1.80 \pm 0.22$	2.128
OM 127	4FGL J1119.0+1235	FSRQ	$2.29 \pm 0.09$	$0.24 \pm 0.06$	$1.21 \pm 0.13$	$2.39 \pm 0.19$	2.126
SDSS J120542.82+332146.9	4FGL J1205.8+3321	BCU	$2.43 \pm 0.17$	-	$0.29 \pm 0.11$	$0.52 \pm 0.19$	2.125
PMN J0124-0624	4FGL J0124.8-0625	BLL	$2.21 \pm 0.12$	-	$0.31 \pm 0.08$	$0.78 \pm 0.22$	2.117
PKS 0227-369	4FGL J0229.5-3644	FSRQ	$2.45 \pm 0.05$	$0.17 \pm 0.04$	$2.19 \pm 0.13$	$3.48 \pm 0.16$	2.115
OF 200	4FGL J0403.3+2601	FSRQ	$2.45 \pm 0.03$	$0.71 \pm 0.02$	$0.19 \pm 0.01$	$0.8 \pm 0.02$	2.109
B3 0803+452	4FGL J0806.5+4503	FSRQ	$2.72 \pm 0.11$	-	$0.79 \pm 0.13$	$1.01 \pm 0.16$	2.102
TXS 0036-099	4FGL J0039.0-0946	FSRQ	$2.83 \pm 0.08$	-	$1.31 \pm 0.15$	$1.54 \pm 0.17$	2.102
4C +01.02	4FGL J0108.6+0134	FSRQ	$2.29 \pm 0.01$	$0.11 \pm 0.01$	$30.88 \pm 0.36$	$66.23 \pm 0.49$	2.099
87GB 145232.0+493854	4FGL J1454.0+4927	BCU	$2.62 \pm 0.18$	-	$0.27 \pm 0.10$	$0.71 \pm 0.22$	2.085
SDSS J105707.47+551032.2	4FGL J1057.2+5510	BLL	$2.02 \pm 0.11$	-	$0.18 \pm 0.05$	$0.37 \pm 0.14$	2.085

<sup>1</sup> The result for this object is listed from the catalogue, as its ROI contains 10 extended sources, which complicates the analysis.

**Table 1.** Table 1 (Continued)

Object	4FGL name	Class	$\alpha_p/\alpha$	$\beta$	Flux	Luminosity	$z$
PKS 1348+007	4FGL J1351.0+0029	FSRQ	$2.43 \pm 0.11$	-	$0.47 \pm 0.11$	$0.80 \pm 0.18$	2.084
PKS B1112-080	4FGL J1114.5-0819	FSRQ	$2.72 \pm 0.02$	$0.12 \pm 0.01$	$1.49 \pm 0.04$	$1.95 \pm 0.21$	2.078
1RXS J032342.6-011131	4FGL J0323.7-0111	BLL	$1.82 \pm 0.07$	$0.08 \pm 0.03$	$0.38 \pm 0.08$	$3.19 \pm 0.36$	2.075
SDSS J100326.63+020455.6	4FGL J1003.4+0205	BCU	$1.66 \pm 0.13$	-	$0.05 \pm 0.02$	$0.75 \pm 0.32$	2.075
PKS 0528+134	4FGL J0530.9+1332	FSRQ	$2.50 \pm 0.03$	$0.23 \pm 0.02$	$4.04 \pm 0.28$	$7.72 \pm 0.42$	2.069
TXS 0322+222	4FGL J0325.7+2225	FSRQ	$2.52 \pm 0.03$	$0.19 \pm 0.03$	$4.78 \pm 0.23$	$7.37 \pm 0.26$	2.066
4C +13.14	4FGL J0231.8+1322	FSRQ	$2.68 \pm 0.01$	-	$2.05 \pm 0.03$	$2.58 \pm 0.03$	2.065
GB6 J1722+6105	4FGL J1722.6+6104	FSRQ	$2.82 \pm 0.15$	$0.09 \pm 0.10$	$0.66 \pm 0.17$	$0.83 \pm 0.16$	2.058
SDSS J000359.23+084138.1	4FGL J0004.0+0840	BLL	$1.79 \pm 0.34$	$0.36 \pm 0.24$	$0.03 \pm 0.02$	$0.55 \pm 0.22$	2.057
87GB 105148.6+222705	4FGL J1054.5+2211	BLL	$2.16 \pm 0.03$	-	$1.76 \pm 0.13$	$4.72 \pm 0.34$	2.055
NVSS J090226+205045	4FGL J0902.4+2051	BLL	$2.06 \pm 0.05$	$0.04 \pm 0.02$	$1.43 \pm 0.15$	$4.72 \pm 0.34$	2.055
PMN J0625-5438	4FGL J0625.8-5441	FSRQ	$2.70 \pm 0.08$	-	$1.20 \pm 0.13$	$1.46 \pm 0.16$	2.051
IVS B0343+485	4FGL J0347.0+4844	FSRQ	$2.47 \pm 0.01$	-	$0.92 \pm 0.03$	$1.40 \pm 0.05$	2.043
GB1 1155+486	4FGL J1158.5+4824	FSRQ	$2.49 \pm 0.05$	-	$1.24 \pm 0.12$	$1.82 \pm 0.17$	2.028
PKS 1318-263	4FGL J1321.3-2641	FSRQ	$2.61 \pm 0.16$	-	$0.62 \pm 0.18$	$0.80 \pm 0.23$	2.027
OX 110	4FGL J2108.5+1434	FSRQ	$2.66 \pm 0.09$	$0.14 \pm 0.08$	$1.26 \pm 0.18$	$1.7 \pm 0.19$	2.017
PKS 0437-454	4FGL J0438.9-4521	BLL	$2.25 \pm 0.06$	$0.11 \pm 0.04$	$1.40 \pm 0.17$	$3.07 \pm 0.21$	2.017
PKS B1412-096	4FGL J1415.9-1002	FSRQ	$0.91 \pm 0.77$	$3.29 \pm 1.20$	$0.06 \pm 0.02$	$0.8 \pm 0.22$	2.001
PKS 0549-575	4FGL J0550.3-5733	FSRQ	$2.23 \pm 0.10$	-	$0.34 \pm 0.08$	$0.73 \pm 0.17$	2.001

monitoring the  $\gamma$ -ray sky since its launch in 2008 (Atwood et al. 2009).

The *Fermi*-LAT PASS8 data collected from August 4, 2008, to December 4, 2022 ( $\sim 14.5$  years), were considered to study the properties of all 79 blazars under consideration. The standard data-reduction procedure was performed following the recommendations from the *Fermi*-LAT science team<sup>1</sup>. For each blazar, events in the energy range between 100 MeV and 500 GeV from a region of interest (ROI) of  $12^\circ$ —reduced to  $10^\circ$  for several sources to better represent the ROI—centered on the  $\gamma$ -ray position of the sources, were downloaded and analyzed. The *Fermi* ScienceTools version 2.0.8 and the P8R3\_SOURCE\_V3 instrument response function were used. To reduce contamination from the Earth’s limb, a zenith angle cut of  $90^\circ$  was applied. Events with a higher probability of being photons were selected using the filter *evclass* = 128 and *evtype* = 3, and the good time intervals were chosen with the expression (DATA\_QUAL > 0)&&(LAT\_CONFIG == 1). The analysis model file was created based on the *Fermi* Fourth Source Catalog (4FGL-DR3 Abdollahi et al. 2022) and includes all sources within an ROI radius plus an additional  $5^\circ$ . During the likelihood fitting, the spectral parameters of all sources within the ROI were allowed to vary, while those of sources outside the ROI were fixed to their 4FGL values. The model file also includes the Galactic diffuse emission model *gll\_iem\_v07* and the isotropic component *iso\_P8R3\_SOURCE\_V3\_v1*. The spectral parameters of the sources, along with the normalization of both background models, were optimized by applying a binned likelihood analysis using the *fermiPy* tool (Wood et al. 2017). The detection significance of the sources is quantified by the likelihood test statistic (TS), defined as  $TS = 2 \times (\log L - \log L_0)$ , where  $L$  is the likelihood with the source at the position of interest included, and  $L_0$  is the likelihood without the source.

The  $\gamma$ -ray variability of the considered sources was investigated by generating light curves in two distinct manners. Initially, for all sources, the 14-year period was divided into equal intervals (e.g., 5, 7, 10 days, depending on the source’s overall detection significance)

to ensure that the light curves did not contain a significant number of upper limits. Within these intervals, the flux and photon index were estimated by applying the unbinned likelihood analysis method. This approach provides a general overview of the flux changes over time, but since the fluxes are averaged over several days, any potential short-scale flux variations are likely to be smoothed out. For a more detailed examination of flux evolution over time, light curves were also generated using the adaptive binning method (Lott et al. 2012), which is applied when photon statistics are sufficient. This technique allows for flexible time bin widths that are determined by assuming a constant uncertainty in the flux estimation. Consequently, brighter source states yield shorter bins, whereas longer bins are used during lower and/or average source states. Light curves produced by this method have been extensively utilized to study short-timescale flux variations in blazar emissions (e.g., see Rani et al. 2013; Britto et al. 2016; Sahakyan & Gasparyan 2017; Zargaryan et al. 2017; Baghmany et al. 2017; Gasparyan et al. 2018; Sahakyan et al. 2018; Sahakyan 2021; Sahakyan et al. 2022b; Sahakyan & Giommi 2022).

### 3.2 NuSTAR

NuSTAR (Harrison et al. 2013) is a hard X-ray telescope operating in the 3-79 keV range, equipped with two focal plane modules: FPMA and FPMB. Among the sources considered, PKS 0528+134, S3 0458-02, PKS 0446+11, PKS 1329-049, 87GB 080551.6+535010, and TXS 0322+222 were observed by NuSTAR once; PKS 2149-306, S5 0212+73, and PKS 0227-369 were observed twice; and 4C +71.07 was observed three times. In total, these amount to 15 observations that provide critical information on the hard X-ray band emission of the sources.

The analysis of all NuSTAR data was performed using the *NuSTAR\_Spectra* pipeline, a shell script built upon the NuSTAR Data Analysis Software (Middei et al. 2022). This script streamlines the process by autonomously retrieving calibrated and filtered event files, employing Ximage for accurate source positioning, and utilizing the *nuproducts* command to retrieve science ready products. Source counts are extracted from a predefined circular region, while background counts are from an annular region, with inner and outer radii

<sup>1</sup> <https://fermi.gsfc.nasa.gov/ssc/data/analysis/documentation/>

sizes dynamically determined by the source’s count rate. Post data selection, the spectra are binned to ensure a minimum of one count per bin, and spectral fitting is executed within the XSPEC framework (Arnaud 1996), applying Cash statistics (Cash 1979) for the energy range from 3 keV to the upper energy limit of detectable signal, which varies between 20 and 79 keV. The fitting is performed using both power-law and log-parabola models, the observed flux in the 3-10 and 10-30 keV bands is estimated and the corresponding SED is computed using the best-fit parameters. Details describing *NuSTAR\_Spectra* pipeline can be found in Middei et al. (2022).

### 3.3 Swift XRT

The high-redshift blazars selected for this study were also frequently monitored by the Swift XRT in the 0.3-10 keV energy range. Of the 79 considered sources, 60 were observed at least once by the Swift telescope. The source PKS 0528+134 was the most frequently observed—141 times—while 4C +71.07, PKS 2149-306, PKS 0226-559, S3 0458-02, 4C +01.02, and PMN J1344-1723 each were observed more than 20 times.

All the Swift XRT data accumulated from the observations of selected sources was retrieved and analyzed using *swift\_xrtproc* script. This automated tool accesses both PC and WT mode observations from Swift XRT and executes the standard analysis procedure which includes the creation of exposure maps, calibration of observational data. The source spectral files are obtained by estimating the source counts within a 20-pixel radius circular region and the background from a surrounding annular region centered on the source. Additionally, it performs corrections for pile-up effects and conducts spectral fitting employing both power-law and log-parabola models within the XSPEC framework. Subsequently, it computes the SED spectral points using the optimal spectral model, computes the flux across specified energy intervals, and estimates the photon index for the selected energy range. For more details on the *swift\_xrtproc* tool see Giommi et al. (2021).

The majority of these sources considered here exhibit no significant variability in the X-ray band, as discussed in the next section, so to enhance the photon statistics and refine the estimation of the X-ray flux, if for a source multiple observations are available, they were combined and analyzed using the tool provided by the UK Swift Science Data Centre (Evans et al. 2009).

### 3.4 Swift UVOT

Together with the XRT, the sources were also observed by Swift UVOT, which provided data in three optical filters (V, B, and U) and three UV filters (W1, M2, and W2). All available Swift UVOT data from the observations of the considered sources were downloaded and analyzed.

The data were analyzed using the *uvotsource* task included in the HEASoft package, version 6.29. Source counts were extracted from a circular region with a radius of 5” centered on the source, while background counts were obtained from a larger circular region with a radius of 20”, located in a nearby source-free area. The observations of all sources were individually checked to ensure the accuracy of source and background region selection. For all sources, the magnitudes were derived using the *uvotsource* tool and corrected for reddening and Galactic extinction using the reddening coefficient  $E(B-V)$  obtained from the Infrared Science Archive<sup>2</sup>. The corrected

fluxes measured for each filter were used to construct the light curves and SEDs. As the considered sources are at high redshift, their optical/UV fluxes could be affected by absorption from neutral hydrogen in intervening *Lyman -  $\alpha$*  absorption systems. These effects were corrected for in the SEDs during theoretical modeling, following the procedures described in Ghisellini et al. (2011) and Ghisellini et al. (2010).

### 3.5 Archival data

To construct the most comprehensive multiwavelength SEDs possible for the considered sources, archival data were also extracted and analyzed in addition to the data discussed herein. This was accomplished using the VOU-Blazar tool (Chang et al. 2020) through Markarian Multiwavelength data center<sup>3</sup>, which retrieves multiwavelength data from 71 catalogs and spectral databases through various online services.

## 4 RESULTS OF DATA ANALYSES

In this section, a comprehensive spectral and temporal analysis of the sources included in our sample are performed. The outcomes of the  $\gamma$ -ray data analysis are provided in Table 1. For each source, the power-law index ( $\alpha_p$ ), or ( $\alpha$ ) together with the curvature parameter ( $\beta$ ) when the data are best described using a low-parabola model, as well as the flux and luminosity (computed from the power-law fit), both with their respective uncertainties and the redshift of each source is reported. When the source spectrum is described by low-parabola model in 4FGL an additional analysis is performed using power-law model.

The analysis results are presented in panel a of Fig. 2, which depicts the flux and photon index derived from a power-law fit. The FSRQs are shown by blue markers, BL Lacs by orange, and BCUs by green. The  $\gamma$ -ray flux of sources within our sample ranges from  $(5.32 \pm 2.25) \times 10^{-10}$  to  $(3.40 \pm 0.02) \times 10^{-7}$  photon  $\text{cm}^{-2} \text{s}^{-1}$ , with the lowest value corresponding to SDSS J100326.63+020455.6 and the highest to 4C +01.02. The mean flux is at  $2.48 \times 10^{-8}$  photon  $\text{cm}^{-2} \text{s}^{-1}$ . The photon index span from  $1.66 \pm 0.12$  to  $3.15 \pm 0.12$ , with the lowest and highest indices observed for SDSS J100326.63+020455.6 and PKS 1915-458, respectively. The FSRQs, which are the most numerous in our sample, largely define these observed ranges. On the other hand, BCUs and BL Lacs exhibit narrower distributions in both  $\gamma$ -ray flux and photon index. Specifically, BL Lacs range between  $(0.18 - 1.86) \times 10^{-8}$  photon  $\text{cm}^{-2} \text{s}^{-1}$  for flux and 1.91–2.62 for photon index, while BCUs between  $(0.05 - 1.60) \times 10^{-8}$  photon  $\text{cm}^{-2} \text{s}^{-1}$  for flux and 1.66–2.73 for photon index. For comparison, blazars with a redshift exceeding 2.5 from Sahakyan et al. (2020) are depicted in light gray in panel a of Fig. 2. This visualization shows that blazars with a redshift beyond 2.5, as well as those included in the current sample, exhibit similar features, occupying similar regions on the photon index versus  $F_\gamma$  plane.

Panel b of Fig. 2 presents the  $\gamma$ -ray luminosity  $L_\gamma$  versus the photon index. This contrasts with the flux, luminosity, on the other hand, accounts for the total energy emitted by the source per unit time, so showing the intrinsic power of the sources. The luminosity of the sources under consideration spans from  $(3.67 \pm 1.37) \times 10^{46}$  erg  $\text{s}^{-1}$  to  $(6.62 \pm 0.05) \times 10^{48}$  erg  $\text{s}^{-1}$ , with the lowest estimated for SDSS J105707.47+551032.2 and the highest for 4C +01.02. Notably,

<sup>2</sup> <http://irsa.ipac.caltech.edu/applications/DUST/>

<sup>3</sup> <https://mmdc.am>

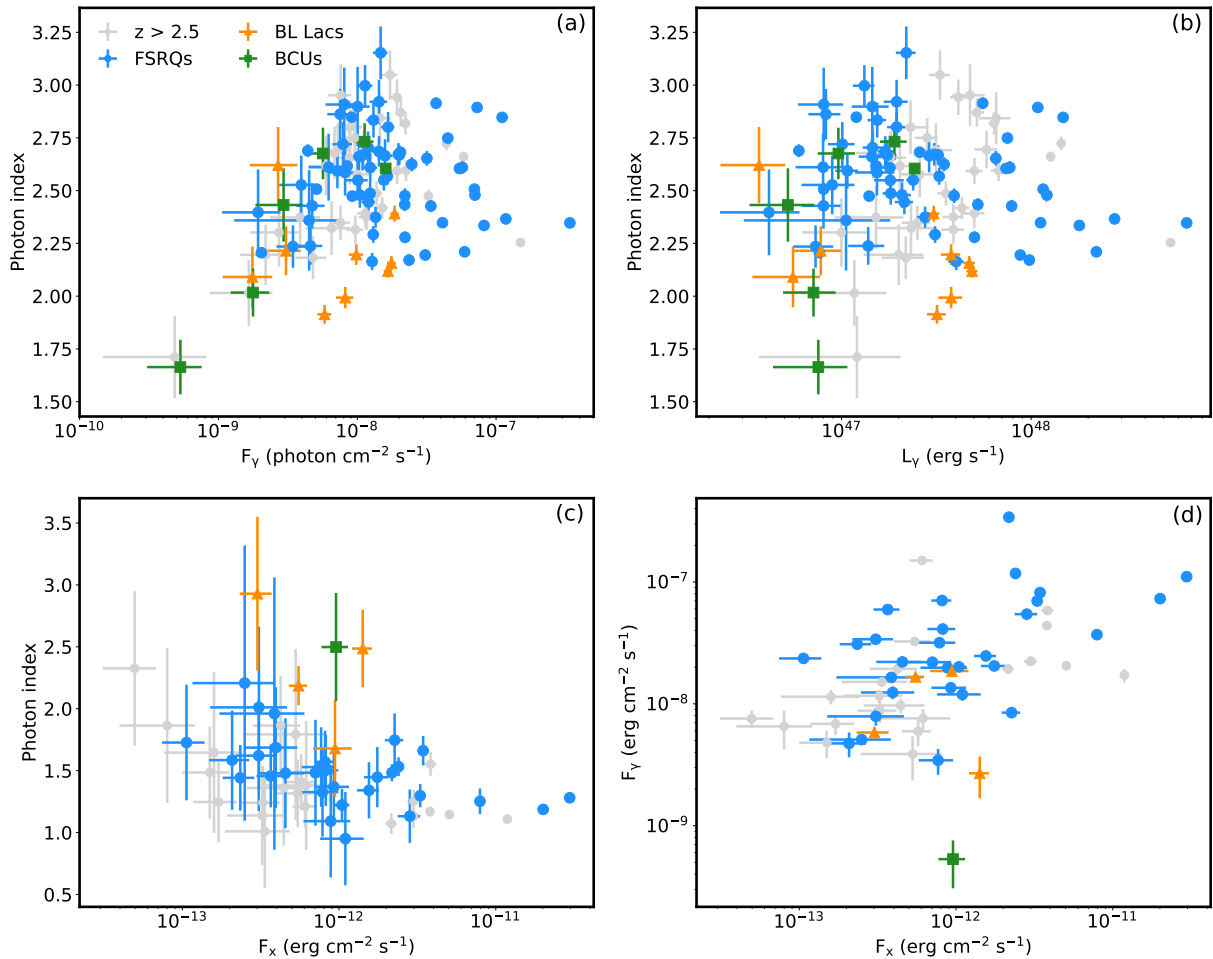


**Figure 2.** Panels (a) and (b): The  $\gamma$ -ray flux ( $> 100$  MeV) and luminosity versus the photon index. Panel (c) The X-ray flux versus the photon index. Panel (d) The X-ray flux versus the  $\gamma$ -ray flux.

the luminosity of 4C +01.02 also exceeds that of B3 1343+451, which is the most luminous in the sample of sources with a redshift beyond 2.5. The range of luminosities for the new sample is slightly shifted towards a higher luminosity range. For instance, the luminosities of PKS 0226-559 ( $2.21 \times 10^{48} \text{ erg s}^{-1}$ ), PKS 0601-70 ( $1.12 \times 10^{48} \text{ erg s}^{-1}$ ), PKS 2149-306 ( $1.09 \times 10^{48} \text{ erg s}^{-1}$ ), S3 0458-02 ( $2.76 \times 10^{48} \text{ erg s}^{-1}$ ), 4C +71.07 ( $1.48 \times 10^{48} \text{ erg s}^{-1}$ ), S4 0917+44 ( $1.80 \times 10^{48} \text{ erg s}^{-1}$ ), PKS 0446+11 ( $1.21 \times 10^{48} \text{ erg s}^{-1}$ ), PKS 1329-049 ( $1.16 \times 10^{48} \text{ erg s}^{-1}$ ), and 4C +01.02 ( $6.62 \times 10^{48} \text{ erg s}^{-1}$ ) are exceeding luminosity of  $10^{48} \text{ erg s}^{-1}$ , making them among the luminous blazars detected in the  $\gamma$ -ray band.

Panel c of Fig. 2 shows the relationship between the X-ray photon index and the flux of the considered sources. The X-ray flux for the sources studied range from  $(1.06 \pm 0.32) \times 10^{-13} \text{ erg cm}^{-2} \text{ s}^{-1}$  for PMN J1344-1723 to  $(2.96 \pm 0.02) \times 10^{-11} \text{ erg cm}^{-2} \text{ s}^{-1}$  for 4C +71.07. The X-ray photon index is predominantly soft (less than 2.0) for the majority of the sources, suggesting that the X-ray emissions are likely dominated by the rising part of inverse Compton component. Notably, the brightest sources in the sample, such as 4C +71.07 and PKS 2149-306, have fluxes of  $(2.96 \pm 0.02) \times 10^{-11} \text{ erg cm}^{-2} \text{ s}^{-1}$  and  $(2.01 \pm 0.04) \times 10^{-11} \text{ erg cm}^{-2} \text{ s}^{-1}$ , with photon indices of  $1.28 \pm 0.01$  and  $1.19 \pm 0.03$ , respectively. These indices indicate their X-ray spectra are particularly hard compared to the rest of the sample. Correspondingly, these two sources also show the highest X-

ray luminosities, being  $(1.13 \pm 0.11) \times 10^{48} \text{ erg s}^{-1}$  for 4C +71.07, and  $(8.79 \pm 1.83) \times 10^{47} \text{ erg s}^{-1}$  for PKS 2149-306.

In panel d of Fig. 2, a comparison of the  $\gamma$ -ray and X-ray fluxes for the selected sources is shown. The wide spread observed in the data suggests that there is no direct or obvious correlation between the  $\gamma$ -ray and X-ray fluxes when considering time-averaged measurements. It should be noted, however, that these are average values and that during shorter time-scale events, such as flares, a correlation may appear. Interestingly, the two brightest in the X-ray band sources, 4C +71.07 and PKS 2149-306, also have notably high  $\gamma$ -ray fluxes of  $(1.11 \pm 0.02) \times 10^{-7} \text{ photon cm}^{-2} \text{ s}^{-1}$  and  $(7.30 \pm 0.20) \times 10^{-8} \text{ photon cm}^{-2} \text{ s}^{-1}$ , respectively. Conversely, the  $\gamma$ -ray bright source 4C +01.02, has only a moderate X-ray flux of  $(2.18 \pm 0.11) \times 10^{-12} \text{ erg cm}^{-2} \text{ s}^{-1}$ , indicating that a high  $\gamma$ -ray flux does not necessarily imply a correspondingly high X-ray flux. This discrepancy shows the complexity of the emission mechanisms and the potential influence of other factors such as beaming, the environment of the source, or the presence of different emission processes at different wavelengths.

The NuSTAR analysis results are presented in Table 2, where for each source the observation sequence, observation time, and flux in the 3 – 10 keV and 10 – 30 keV ranges, along with the photon index are provided. Three NuSTAR observations (60160099002 for S5 0212+73, 60002045002 for 4C +71.07, and 60367002002 for PKS 0227-369) were relatively short (on the order of a few hundred sec-

onds), and hence no spectral analysis was conducted. In the 3 – 10 keV range, the highest flux of  $(2.02 \pm 0.01) \times 10^{-11}$  erg cm<sup>-2</sup> s<sup>-1</sup> was observed for 4C +71.07 on MJD 56675.22, while the lowest flux of  $(1.95 \pm 0.27) \times 10^{-13}$  erg cm<sup>-2</sup> s<sup>-1</sup> was observed for 87GB 080551.6+535010. The photon index for all considered sources is hard, ranging from 1.09 to 1.67, suggesting that the hard X-ray component corresponds to the rising part of the inverse Compton component. The variability of the 3 – 10 keV and 10 – 30 keV fluxes could only be investigated for 4C +71.07 and PKS 2149-306, as multiple observations in different periods are available; however, the flux remained relatively stable.

#### 4.1 $\gamma$ -ray variability

The use of adaptive binning methods for computing light curves allowed detailed investigation of the  $\gamma$ -ray flux variation of considered sources. Flux variations, characterized by several times increases from average levels, have been observed in 31 sources. The most variable sources in the  $\gamma$ -ray band, where multiple flaring activities have been observed, are PKS 0226-559, PKS 2149-306, S3 0458-02, 4C+71.07, S4 0917+44, PKS 1329-049 and 4C+01.02. For example, the adaptively binned  $\gamma$ -ray light curve of PKS 0226-559, the most distant source in our sample at a redshift  $z = 2.464$  showing variability, computed for energies above 239.66 MeV, is displayed in panel a) of Fig. 3. From the start of *Fermi*-LAT observations until MJD 55504 (November 04, 2010), the  $\gamma$ -ray emission of this source was in a low state being  $(4.89 \pm 0.71) \times 10^{-9}$  photon cm<sup>-2</sup> s<sup>-1</sup>. Subsequent periods of flaring activity occurred between MJD 55504.30-55584.50, 56153.18-57472.15, and MJD 58084.93-58664.52. During its most active state, between MJD 58084.93 and 58664.52, the maximum flux was  $(3.99 \pm 0.67) \times 10^{-7}$  photon cm<sup>-2</sup> s<sup>-1</sup> observed on MJD 58507.69. Also, the luminosity of the source significantly increased during these flaring periods. While the long-term averaged luminosity was  $(1.76 \pm 0.04) \times 10^{48}$  erg s<sup>-1</sup>, the luminosity during flares exceeded  $10^{49}$  erg s<sup>-1</sup>. For example, the source luminosity was  $> 10^{49}$  erg s<sup>-1</sup> 42 times, with the peak luminosity of  $(5.33 \pm 0.92) \times 10^{49}$  erg s<sup>-1</sup> observed on MJD 58167.46.

Among the flaring sources, significant increases in  $\gamma$ -ray emission have been observed for PKS 2149-306, 4C+71.07, PKS 1329-049, and 4C+01.02. For example, the time-averaged  $\gamma$ -ray flux of PKS 2149-306 ( $z = 2.345$ ) is  $(2.01 \pm 0.47) \times 10^{-7}$  photon cm<sup>-2</sup> s<sup>-1</sup>, but there was a notable period of elevated  $\gamma$ -ray emission between MJD 56288.92 and 56444.75 (Fig. 3 panel b). During this interval, the flux above 144.85 MeV exceeded  $10^{-6}$  photon cm<sup>-2</sup> s<sup>-1</sup> on eight time intervals. The peak flux during this period was  $(1.68 \pm 0.33) \times 10^{-6}$  photon cm<sup>-2</sup> s<sup>-1</sup> observed on MJD 56302.61. Additionally, the source exhibited another active  $\gamma$ -ray emission state between MJD 55554.39 and 55650.67. In this period, the  $\gamma$ -ray flux consistently exceeded  $10^{-7}$  photon cm<sup>-2</sup> s<sup>-1</sup>, with a maximum of  $(7.08 \pm 1.22) \times 10^{-7}$  photon cm<sup>-2</sup> s<sup>-1</sup> observed on MJD 55613.98. During multiple flaring periods of 4C+71.07 (Fig. 3 panel d), which is at a redshift of  $z = 2.218$ , the  $\gamma$ -ray emission notably exceeded its time-averaged flux of  $(1.06 \pm 0.01) \times 10^{-7}$  photon cm<sup>-2</sup> s<sup>-1</sup>. Specifically, in three distinct flaring periods—MJD 55862.01-55932.97, MJD 57227-57245.79, and MJD 57296.92-57338.47—the flux above 138.16 MeV exceeded  $10^{-6}$  photon cm<sup>-2</sup> s<sup>-1</sup>. The peak flux during these flaring events was at  $(8.02 \pm 1.40) \times 10^{-6}$  photon cm<sup>-2</sup> s<sup>-1</sup>, and was observed on MJD 57335.21. The  $\gamma$ -ray emission of PKS 1329-049, with a redshift of  $z = 2.15$ , is predominantly in its average emission state, as depicted in Fig. 3 panel f). However, it exhibited an elevated emission state during the period from MJD 55442.09 to 55507.87 when the peak flux reached  $(2.71 \pm 0.52) \times 10^{-6}$  photon cm<sup>-2</sup> s<sup>-1</sup>

observed on MJD 55445.32. In contrast, 4C+01.02, with a redshift of  $z = 2.099$ , experiences alternating periods of flaring activity, with the most intense  $\gamma$ -ray flares observed after MJD 57000. The source entered an active  $\gamma$ -ray emission state starting from MJD 59615.91, when the peak  $\gamma$ -ray flux, measured above 171.79 MeV, reached  $(2.92 \pm 0.50) \times 10^{-6}$  photon cm<sup>-2</sup> s<sup>-1</sup> on MJD 59663.19. The other two sources, depicted in panels c) and e) of Fig. 3, also exhibit multiple flaring periods but with only modest increases in their  $\gamma$ -ray flux. Specifically, the peak  $\gamma$ -ray flux of S3 0458-02, measured above 202.55 MeV, was  $(8.32 \pm 1.41) \times 10^{-7}$  photon cm<sup>-2</sup> s<sup>-1</sup> observed on MJD 57258.92. Similarly, for S4 0917+44, it was  $(4.27 \pm 0.75) \times 10^{-7}$  photon cm<sup>-2</sup> s<sup>-1</sup> observed on MJD 57946.70.

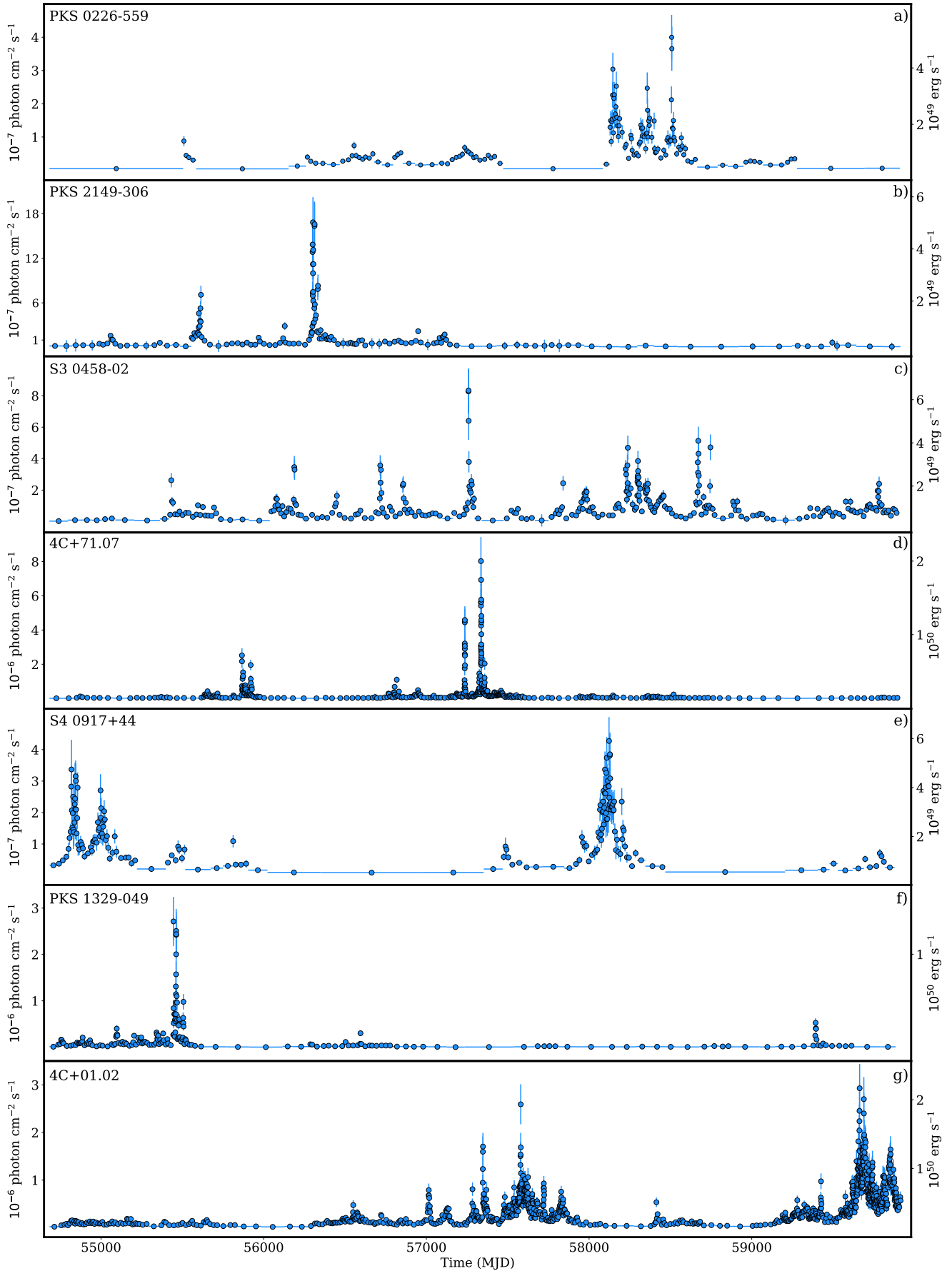
Especially profound is the luminosity increase in 4C+71.07, PKS 1329-049, and 4C+01.02 (see Fig. 3). For 4C+71.07, during the flaring periods in MJD 57227-57245.79 and MJD 57296.92-57338.47, the source luminosity exceeded  $10^{50}$  erg s<sup>-1</sup> 11 times. The highest luminosity of  $(2.03 \pm 0.36) \times 10^{50}$  erg s<sup>-1</sup> was observed on MJD 57335.21. PKS 1329-049 was in an extreme bright state on MJD 55445.23 and MJD 55468.18, with luminosities of  $(1.07 \pm 0.21) \times 10^{50}$  erg s<sup>-1</sup> and  $(1.39 \pm 0.26) \times 10^{50}$  erg s<sup>-1</sup>, respectively. Similarly, 4C+01.02 was in an extreme bright state between MJD 59662.03-59663.55, during which in 6 consecutive bins the flux exceeded  $10^{50}$  erg s<sup>-1</sup>, with the highest flux of  $(2.08 \pm 0.48) \times 10^{50}$  erg s<sup>-1</sup> observed on MJD 59662.62. Because of such elevated luminosity, 4C+71.07, PKS 1329-049, and 4C+01.02 rank among the sources with the highest luminosity in the  $\gamma$ -ray band.

In Fig. 4, the  $\gamma$ -ray light curves for 4C+13.14, 87GB 080551.6+535010, B2 1436+37B, PKS 0227-369, PKS 0528+134, PKS 0446+11, PKS 0601-70, S5 1053+70, and TXS 0322+222 are presented. For the majority of the time, the emission from these objects remains in a low to average state. However, during certain flaring periods, their  $\gamma$ -ray emission shows modest increases. These sources are typically weak, with  $\gamma$ -ray fluxes generally on the order of  $10^{-8}$  photon cm<sup>-2</sup> s<sup>-1</sup>, but there are instances when the flux exceeds  $10^{-7}$  photon cm<sup>-2</sup> s<sup>-1</sup>. For example, during an elevated  $\gamma$ -ray emission state, the peak flux of S5 1053+70 above 179.20 MeV was  $(1.42 \pm 0.24) \times 10^{-7}$  photon cm<sup>-2</sup> s<sup>-1</sup> observed on MJD 57684.01. Similarly, for PKS 0601-70, the highest  $\gamma$ -ray flux reached  $(1.64 \pm 0.30) \times 10^{-7}$  photon cm<sup>-2</sup> s<sup>-1</sup> on MJD 55136.37. For PKS 0446+11, the peak  $\gamma$ -ray flux was  $(1.77 \pm 0.34) \times 10^{-7}$  photon cm<sup>-2</sup> s<sup>-1</sup> observed on MJD 55304.46, and so on.

#### 4.2 X-ray variability

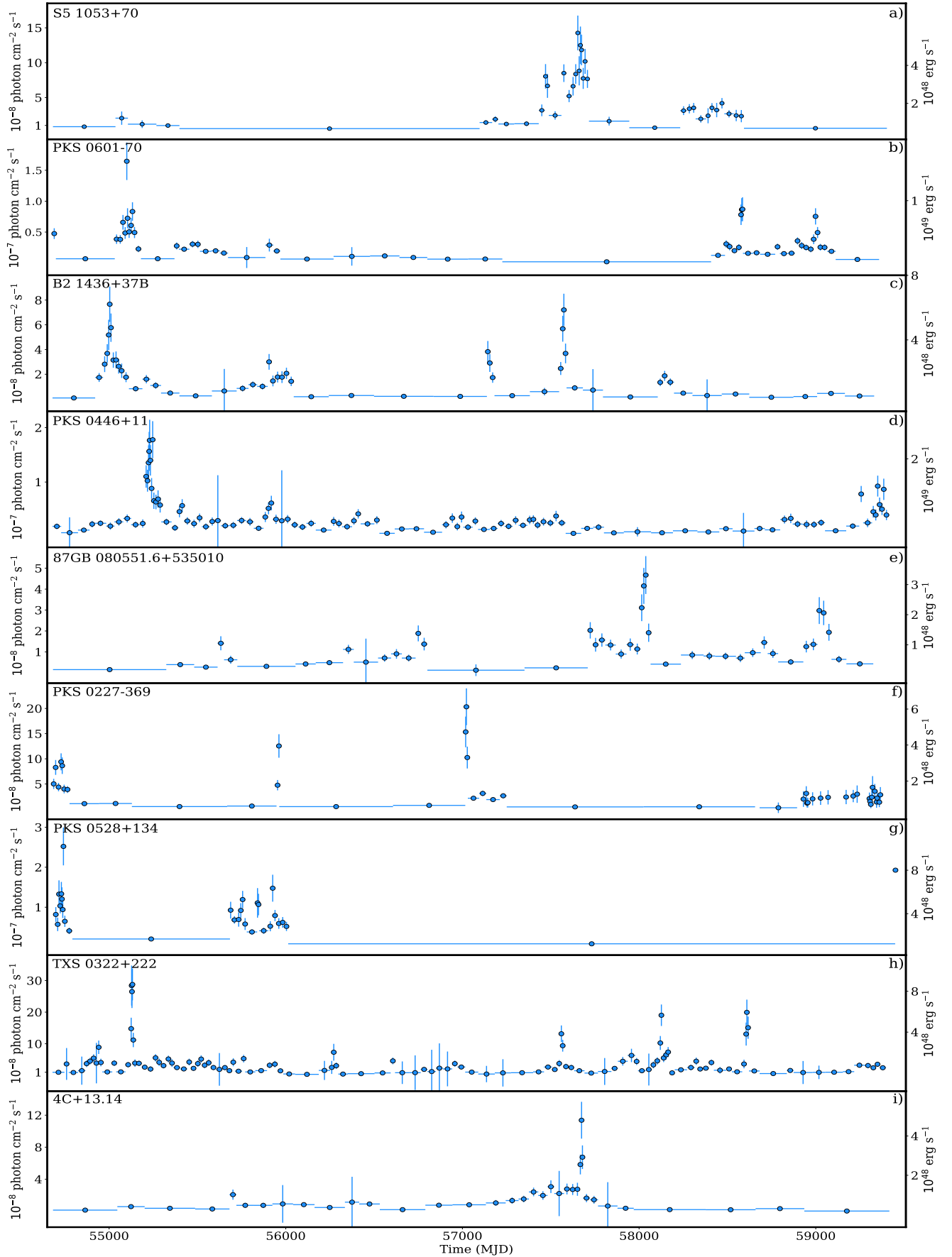
In the considered source sample, some of the sources were observed multiple times by the Swift telescope, permitting investigation of the temporal variability of X-ray flux across different years. Among the sources considered, variability in X-ray flux was observed in 4C +71.07, PKS 0226-559, PKS 1329-049, PKS 2149-306, S3 0458-02 and S4 0917+44. For PKS 0226-559 and S4 0917+44, a limited number of observations were available but the ratio between the maximum and minimum fluxes is approximately 3 – 4, indicating temporal flux variability.

The X-ray flux variations for 4C +71.07 (blue) and PKS 2149-306 (green) are shown in the upper panel of Fig. 5. For 4C +71.07, the lowest observed X-ray flux was  $(1.00 \pm 0.12) \times 10^{-11}$  erg cm<sup>-2</sup> s<sup>-1</sup> on MJD 55247.68, while the highest was  $(5.63 \pm 1.02) \times 10^{-11}$  erg cm<sup>-2</sup> s<sup>-1</sup> on MJD 56832.97. Elevated X-ray emission states for this source were observed around MJD 56000 and MJD 57000, during which most of the X-ray observations were performed. Conversely, PKS 2149-306 exhibited



**Figure 3.** The  $\gamma$ -ray light curve of the sources considered in this study, which show a high amplitude  $\gamma$ -ray flux increase during the flares. The left axis shows the variation of flux over time, while the right axis displays the luminosity.  
MNRAS **000**, 1–20 (2022)

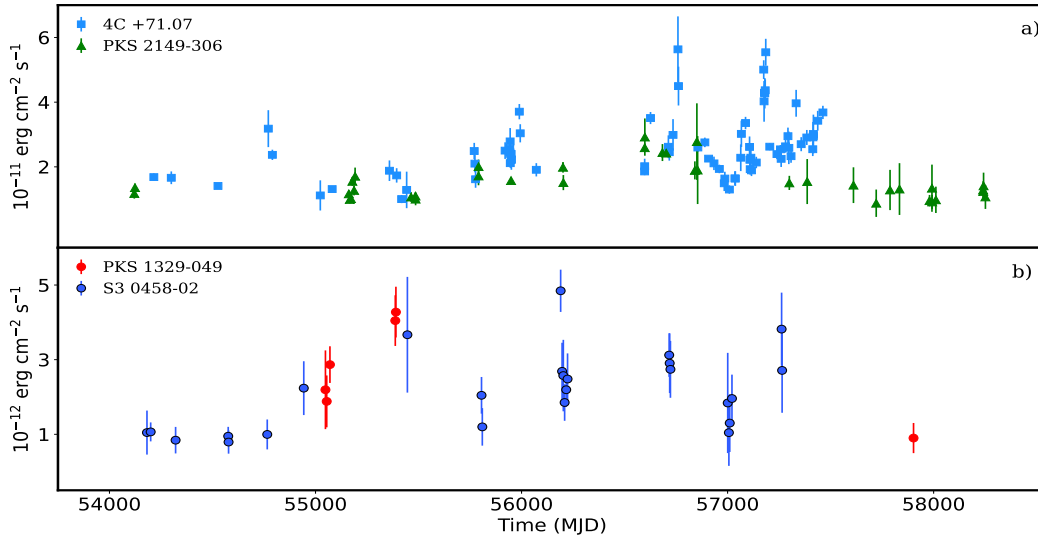




**Figure 4.** The  $\gamma$ -ray light curve of the sources analyzed in this study, which show a modest amplitude  $\gamma$ -ray flux increase during the flares. The left and right axes are the same as in Figure 3.

**Table 2.** NuSTAR analysis results. The source name, NuSTAR sequence ID, observation time in MJD, the logarithm of the 3-10 keV ( $\log F_{3-10}$ ) and 10-30 keV ( $\log F_{10-30}$ ) bands flux and the photon index for each observation are given.

Source	Sequence ID	MJD	$\log F_{3-10}$	$\log F_{10-30}$	photon index
4C +71.07	60002045004	56675.22	$-10.70 \pm 0.003$	$-10.55 \pm 0.005$	$1.63 \pm 0.01$
4C +71.07	60002045002	56641.65	$-10.88 \pm 0.004$	$-10.75 \pm 0.007$	$1.67 \pm 0.02$
PKS 2149-306	60001099002	56643.22	$-10.71 \pm 0.003$	$-10.43 \pm 0.003$	$1.35 \pm 0.01$
PKS 2149-306	60001099004	56765.64	$-10.79 \pm 0.003$	$-10.55 \pm 0.004$	$1.45 \pm 0.01$
S3 0458-02	60367003001	58234.31	$-11.65 \pm 0.014$	$-11.51 \pm 0.020$	$1.64 \pm 0.08$
87GB 080551.6+535010	80001004002	56785.45	$-12.71 \pm 0.061$	$-12.30 \pm 0.087$	$1.09 \pm 0.28$
PKS 0446+11	60101078002	57358.10	$-12.53 \pm 0.059$	$-12.37 \pm 0.088$	$1.60 \pm 0.29$
TXS 0322+222	60101079002	57334.11	$-11.88 \pm 0.017$	$-11.54 \pm 0.027$	$1.24 \pm 0.09$
PKS 0528+134	60160238002	58509.08	$-12.09 \pm 0.034$	$-11.94 \pm 0.040$	$1.61 \pm 0.16$
PKS 0227-369	60367002002	57975.49	$-12.56 \pm 0.055$	$-12.27 \pm 0.077$	$1.34 \pm 0.29$
PKS 1329-049	60160541002	57902.35	$-12.27 \pm 0.043$	$-12.03 \pm 0.050$	$1.44 \pm 0.19$
S5 0212+73	60160099002	57442.46	$-11.24 \pm 0.006$	$-11.03 \pm 0.009$	$1.52 \pm 0.03$

**Figure 5.** The X-ray light curve of 4C +71.07, PKS 2149-306, PKS 1329-049, and S3 0458-02, each with multiple X-ray observations, exhibits noticeable variability.

lower amplitude flux changes, with its highest X-ray flux being  $(2.92 \pm 0.58) \times 10^{-11} \text{ erg cm}^{-2} \text{ s}^{-1}$ , observed on MJD 56643.02. The lower panel of Fig. 5 shows the X-ray flux variations for PKS 1329-048 (red) and S3 0458-02 (blue). Initially, the X-ray emission for S3 0458-02 was on the order of  $\sim 10^{-12} \text{ erg cm}^{-2} \text{ s}^{-1}$ , but it increased to approximately  $\sim 5 \times 10^{-12} \text{ erg cm}^{-2} \text{ s}^{-1}$  around MJD 56200. For PKS 1329-048, the observed highest X-ray flux was  $(4.28 \pm 0.68) \times 10^{-12} \text{ erg cm}^{-2} \text{ s}^{-1}$  on MJD 55390.19, whereas it decreased to  $(8.99 \pm 4.03) \times 10^{-13} \text{ erg cm}^{-2} \text{ s}^{-1}$  on MJD 57902.45.

### 4.3 Variability in optical/UV bands

The observations from the Swift UVOT of selected sources allows to study the flux variability within the optical/UV bands. Investigating variability is challenging when the number of observations is limited, as changes in flux up to a factor of 2 can be observed across different filters; however, this does not provide a comprehensive understanding of the flux changes in time. Notably, clear flux variability is evident in the emissions from 4C+01.02, PKS 0226-559, and PKS 2149-306. For 4C+01.02, the initial flux measurements in the V, B, and U filters are approximately  $10^{-12} \text{ erg cm}^{-2} \text{ s}^{-1}$ , and approximately  $2 \times 10^{-13} \text{ erg cm}^{-2} \text{ s}^{-1}$  in the W1, W2, and M2 fil-

ters. After MJD 56500, the source exhibits increased flux across all filters during several observations. The highest observed flux in the B filter was  $(3.91 \pm 0.33) \times 10^{-12} \text{ erg cm}^{-2} \text{ s}^{-1}$  on MJD 57363.45. For PKS 0226-559, the mean flux is  $\sim 5 \times 10^{-13} \text{ erg cm}^{-2} \text{ s}^{-1}$ , but the flux in V filter increased up to  $(3.1 - 0.46) \times 10^{-12} \text{ erg cm}^{-2} \text{ s}^{-1}$  during the flare on MJD 58161.21. The UV emission from PKS 2149-306, in the W1, W2, and M2 filters, remains relatively stable across various observations, whereas the optical emission (V, B, and U) shows variability. Specifically, on MJD 53717.92, MJD 54980.86, and MJD 58586.29, the flux increased to approximately  $3 \times 10^{-12} \text{ erg cm}^{-2} \text{ s}^{-1}$ , with the lowest observed flux being around  $10^{-13} \text{ erg cm}^{-2} \text{ s}^{-1}$ .

## 5 MODELING OF MULTIWAVELENGTH SEDS

The data analyzed in this study, combined with those collected from the archives, enabled to construct the SEDs for the selected sources from the radio to the HE  $\gamma$ -ray bands. The multiwavelength SEDs are presented in Fig. 6 where the data analyzed in this work are highlighted in different colors (see the legend), while archival data retrieved using the VOU-Blazar tool are depicted in gray. All the

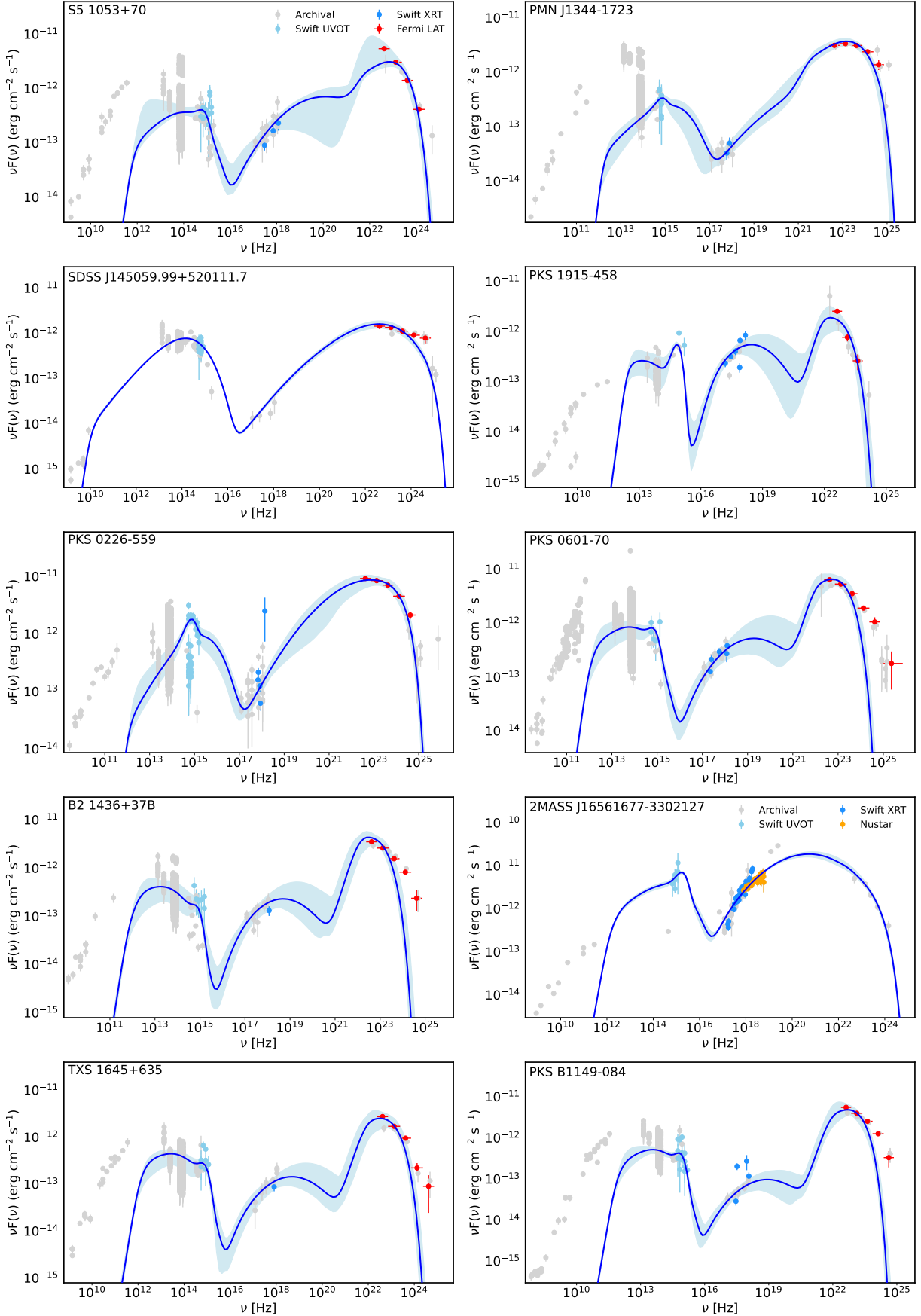


**Figure 6.** The broadband SED modeling results for the sources under consideration. The data analyzed from Swift UVOT, XRT, NuSTAR, and Fermi-LAT observation are depicted in cyan, blue, orange, and red, respectively, while archival data are shown in gray. The blue line represents the combined contribution of the synchrotron, disk, SSC, and EIC-BLR components. The blue shaded area indicates the region of uncertainty associated with the model.

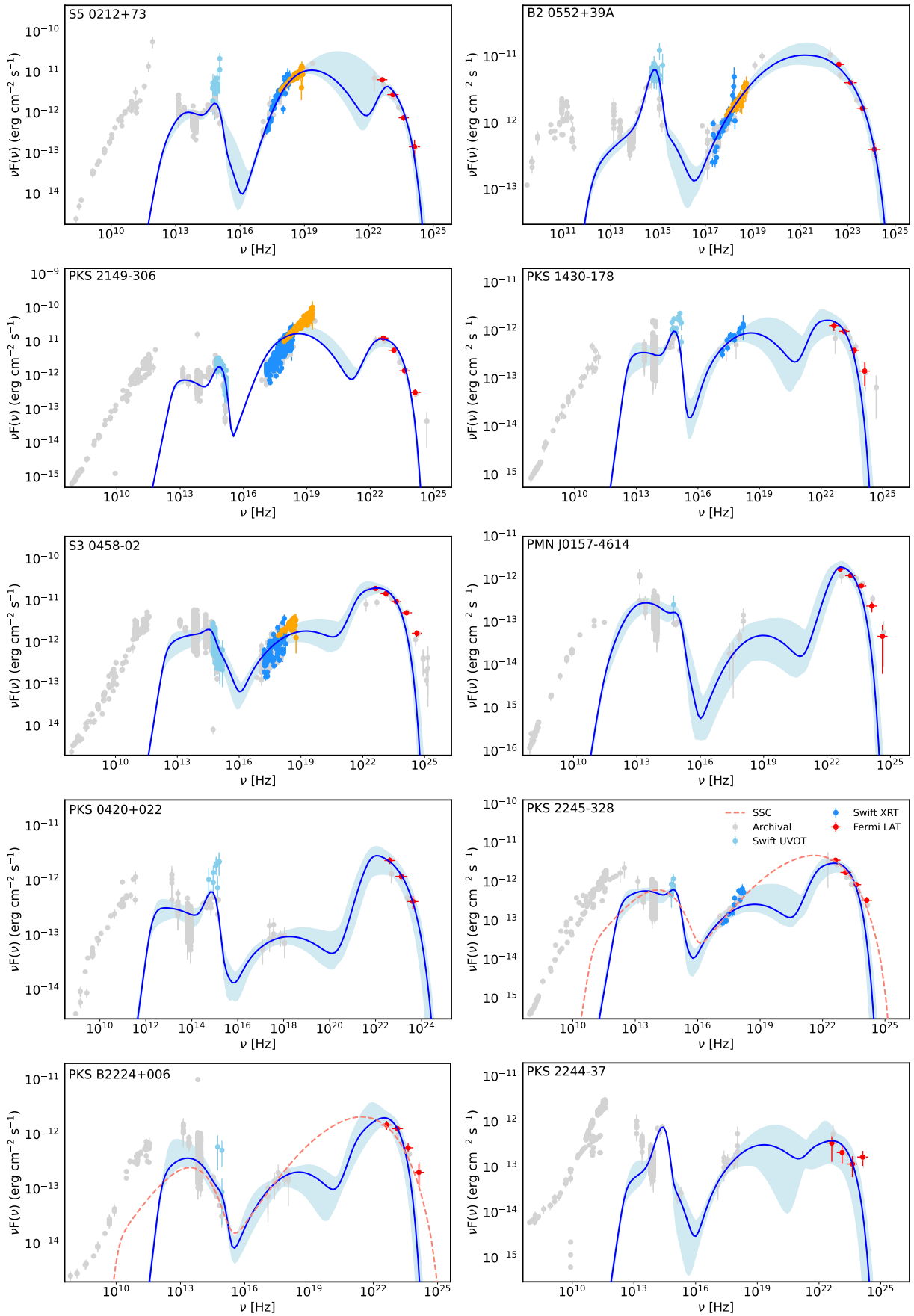


Figure 6. (continued)

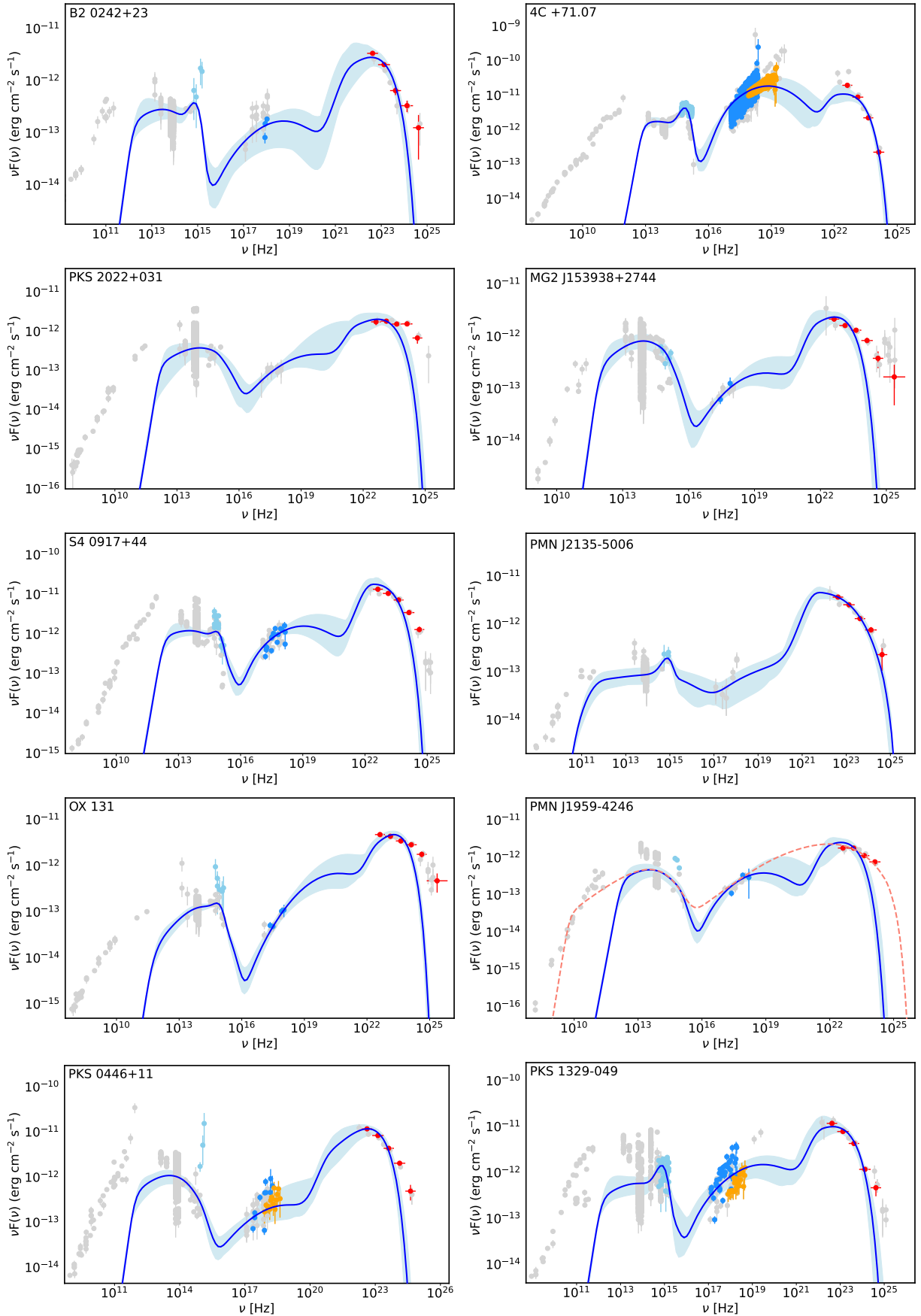


Figure 6. (continued)

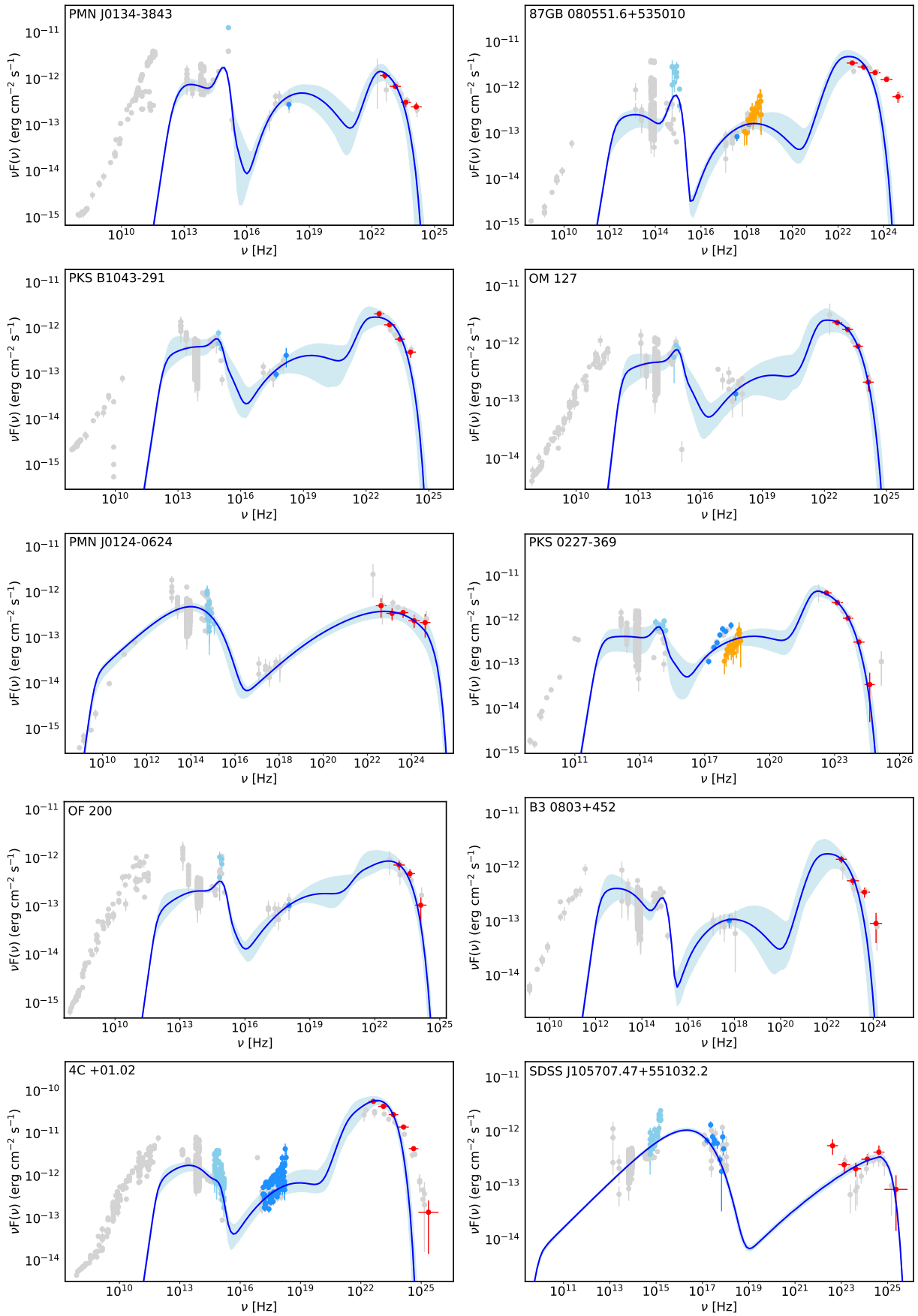


Figure 6. (continued)

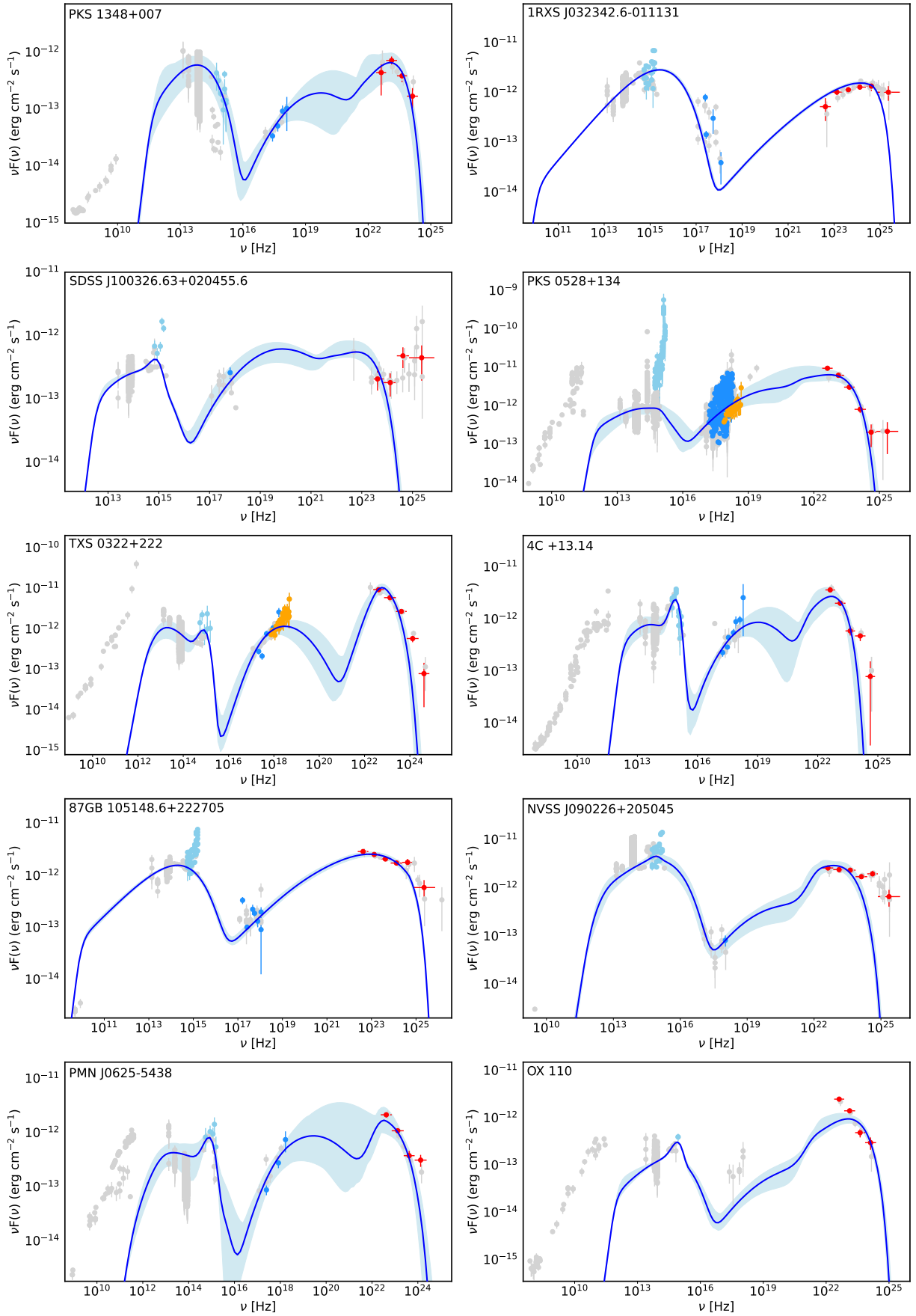


Figure 6. (continued)

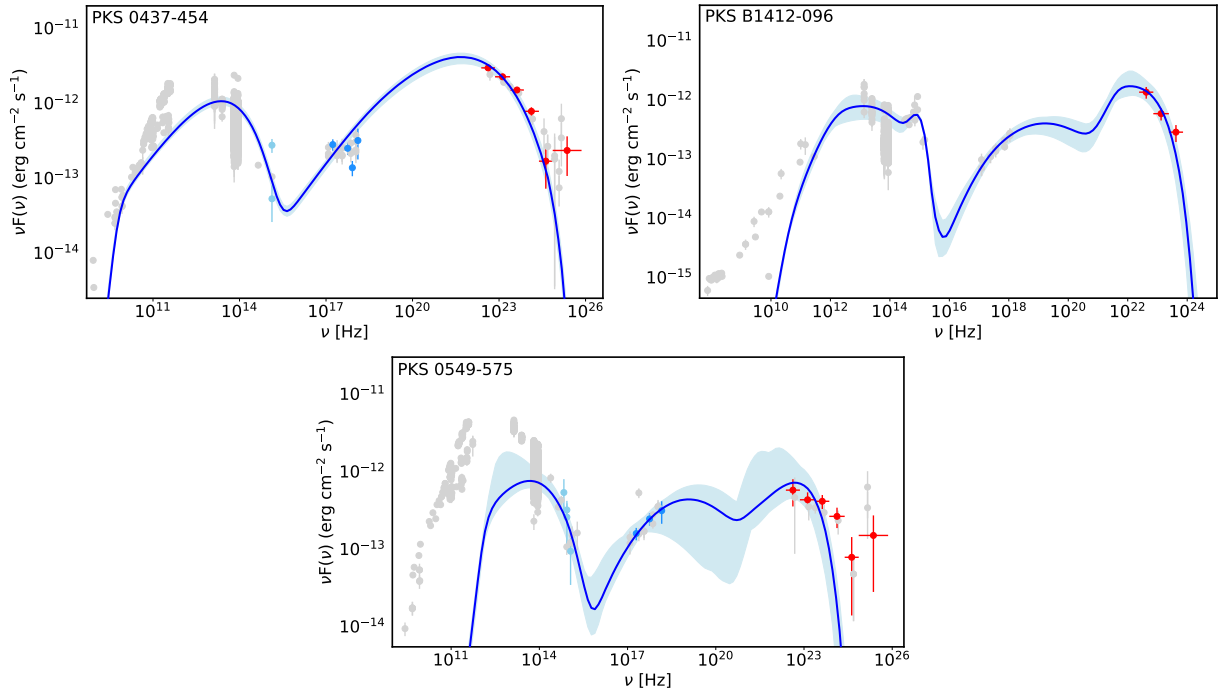


Figure 6. (continued)

SEDs exhibit the traditional double-humped structure with a clear Compton dominance (i.e., the Compton peak luminosity is significantly higher than the synchrotron peak luminosity).

The selected SEDs were modeled using a leptonic one-zone synchrotron and inverse Compton model. In this scenario, the emission region is assumed to be located at a distance  $R_{\text{dis}}$  from the central black hole and is assumed to have a spherical geometry with a radius  $R$ . This region moves along the jet with a bulk Lorentz factor  $\Gamma$  and is observed at a small viewing angle, resulting in the amplification of radiation by a factor of  $\delta \approx \Gamma$ . The emitting region is populated with nonthermal particles (electrons and positrons), whose energy distribution follows a power law with an exponential cutoff described as:

$$N(\gamma) = N_0 \gamma^{-p} e^{-\gamma/\gamma_{\text{cut}}} \quad \text{for } \gamma > \gamma_{\text{min}} \quad (1)$$

where  $p$  is the spectral index of the power-law distribution for the emitting electrons,  $\gamma_{\text{cut}}$  is the cutoff Lorentz factor, and  $\gamma_{\text{min}}$  represents the minimum energy. Here,  $N_0$  denotes the normalization constant of the electron distribution, which defines the total energy content of the electrons as given by  $U_e = mc^2 \int \gamma N(\gamma) d\gamma$ .

Within the emitting region (blob), electrons lose energy through synchrotron emission under the magnetic field  $B$ , resulting in the first bump in the multiwavelength SED. The second bump is attributed to inverse Compton scattering of low-energy photons, which may originate either internally or externally to the jet. Synchrotron photons can be inverse Compton scattered to higher energies via SSC radiation (Ghisellini et al. 1985; Maraschi et al. 1992; Bloom & Marscher 1996), and the inverse Compton scattering of external photons may also contribute to the formation of the second component. Depending on the emitting region's proximity to the central black hole, different low-energy photon fields can be inverse Compton up-scattered: photons directly from the accretion disk (Dermer et al. 1992; Dermer & Schlickeiser 1994), photons reprocessed by the BLR (Sikora et al. 1994), or photons from the dusty torus (Błażejowski et al. 2000).

In the current study, we assume that the emitting region is within the BLR ( $R_{\text{dis}} < R$ ), and that accretion disk photons reprocessed by the BLR (EIC-BLR) alongside synchrotron photons are the primary targets for inverse Compton scattering. However, we note that alternative scenarios, wherein the emitting region lies significantly closer to the central black hole or outside the BLR, cannot be excluded. Constraining the location of the emitting region requires high-quality and high-resolution data at low energy bands, which is unavailable for distant blazars and falls outside the scope of this study.

During the modeling, the accretion disk luminosity ( $L_{\text{disk}}$ ) and the temperature (energy) of the photons were estimated by fitting the UV band's excess emission with a blackbody component. If the thermal component could not be distinguished, an upper limit was established by ensuring that the disk's emission does not outshine the observed nonthermal emission from the jet. With  $L_{\text{disk}}$ , the radius of the BLR is calculated using the relation  $R_{\text{BLR}} = 10^{17} L_{45, \text{disk}}$  (Ghisellini & Tavecchio 2015). Subsequently, the BLR is represented as a spherical shell, with an inner boundary of  $R_{\text{in, BLR}} = 0.9 \times R_{\text{BLR}}$  and an outer boundary of  $R_{\text{out, BLR}} = 1.2 \times R_{\text{BLR}}$ .

The SEDs were fitted using the publicly available JetSet code (Massaro et al. 2006; Tramacere et al. 2009, 2011; Tramacere 2020), which facilitates the comparison of numerical models with observed data. For the FSRQs, the synchrotron/EIC-BLR model was used, while for the BL Lacs, the synchrotron/SSC model. Only one BCU has sufficient data for the modeling, SDSS J100326.63+020455 which was also modeling using synchrotron/SSC-BLR modeling considering the shape of the SED. The model consists of a combined contribution from synchrotron, disk, SSC, and EIC-BLR components, which are optimized during the fitting process. The free parameters in the model are the spectral index ( $p$ ), the cutoff Lorentz factor ( $\gamma_{\text{cut}}$ ), the minimum Lorentz factor ( $\gamma_{\text{min}}$ ), the magnetic field ( $B$ ), the Doppler factor ( $\delta$ ), the size of the emitting region ( $R$ ), and the energy density of the electrons ( $U_e$ ). Optimization is performed in two stages: initial fitting is done with the Minuit optimizer, fol-



lowed by refinement using the Markov Chain Monte Carlo method. We note that  $R$  can also be constrained by variability considerations. However, due to insufficient data for all sources, variability analysis could not be conducted. Therefore, during the fitting process,  $R$  was treated as a parameter dependent on the variability timescale ( $t_{\text{var}}$ ) and  $\delta$ , via the relation  $R = \delta c t_{\text{var}} / (1 + z)$ , with  $t_{\text{var}}$  assumed to be within a 0.1 to 7-day range. However, we refrain from commenting on  $t_{\text{var}}$  (and consequently  $R$ ) as it can only be accurately determined with high-quality data. The pair-production absorption effect due to interaction with EBL photons was incorporated using the model of Franceschini et al. (2008).

## 6 RESULTS

The modeling results are shown in Fig. 6 and the results are given in Table 3. For this modeling, we selected only those sources with sufficient data, particularly those having the X-ray data, as the HE component cannot be constrained without them. There is significant amplitude variability in some sources across optical, IR, and X-ray bands (e.g., PKS 1329-049, PKS 0446+11, 4C +01.02, etc.), which our current modeling does not adequately interpret. To accurately model these flaring periods, a careful selection of (quasi) contemporaneous data is required. However, this is beyond the scope of the current paper, whose primary aim is to estimate the time-averaged properties of the selected sources.

The EIC-BLR model was used to model all the SED of all FSRQs (46 sources). In Fig. 6, the sum of all components – the combined contribution of the synchrotron, disk, SSC, and EIC-BLR components – is depicted in blue. The emission at lower energy bands (up to X-rays) is dominated by the synchrotron and disk components, while at HEs, the SSC and EIC-BLR components are dominant. The modeling facilitates the estimation of parameters describing the jet ( $B$ ,  $\delta$ ) as well as those characterizing the emitting electrons ( $p$ ,  $\gamma_{\text{min}}$ , and  $\gamma_{\text{cut}}$ ). From the modeling of the SEDs of the FSRQs, the power-law index of the electrons varies within a range from  $p = 1.56$  to  $p = 2.85$ , predominantly constrained by the SSC fit of the X-ray data. The hardest spectral indices are observed in sources lacking high-quality X-ray data. For instance,  $p = 1.56 \pm 0.064$  for PKS 0226-559,  $p = 1.60 \pm 0.12$  for OX 131, and  $p = 1.70 \pm 0.21$  for PKS 1348+007, etc. The power-law index of the electrons, inferred from the SSC fitting of BL Lacs (7 sources), is harder than that for FSRQs, ranging between 1.71 and 2.25. Relatively hard indices of  $1.71 \pm 0.01$  and  $1.79 \pm 0.01$  were estimated for SDSS J145059.99+520111.7 and NVSS J090226+205045, respectively.

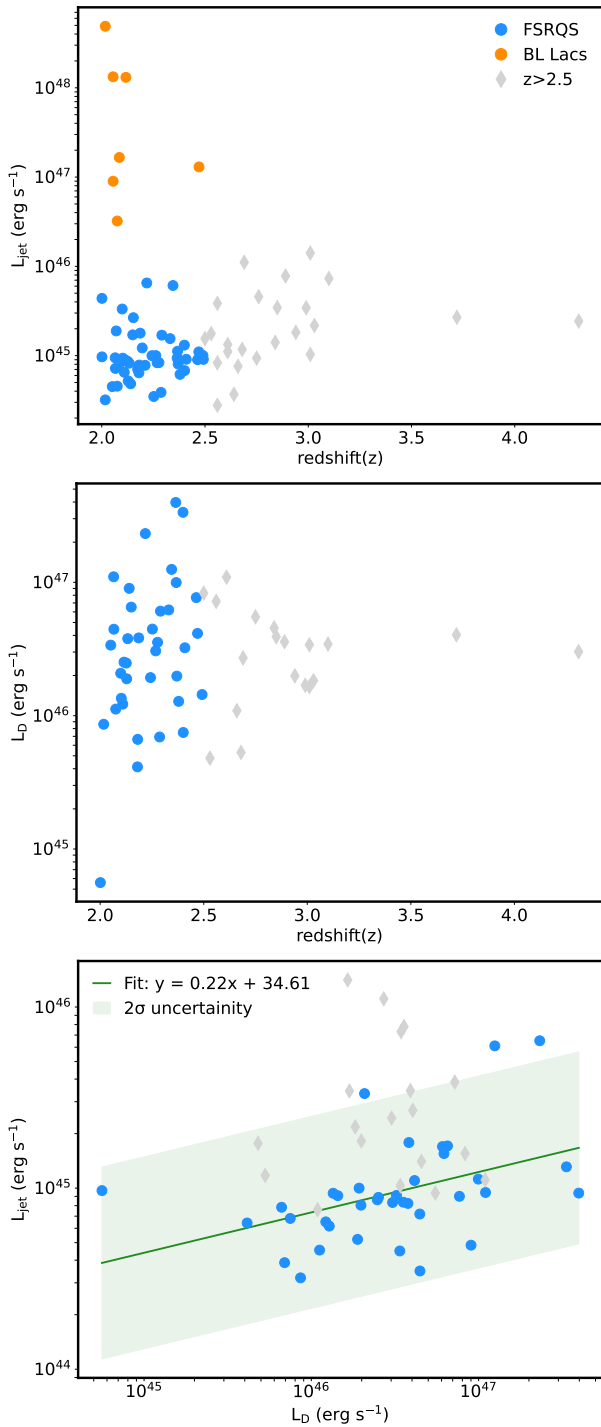
For the FSRQs, the cutoff Lorentz factor ( $\gamma_{\text{cut}}$ ) for the considered sources varies within a range from 237.6 to  $3.53 \times 10^3$ , determined by the optical/UV and/or X-ray data. A high value of  $(3.55 \pm 0.49) \times 10^4$  was estimated for PMN J2135-5006, which has sparse X-ray data and is therefore not considered in the discussions. The lowest value of  $237.6 \pm 21.8$  was estimated for TXS 0322+222, as the shape of the low-energy data (below optical) and the optical/UV data impose a strong constraint on this parameter. A comparably high cutoff Lorentz factor,  $\gamma_{\text{cut}} = (3.53 \pm 0.31) \times 10^3$ , was estimated for PMN J1344-1723. In the modeling of BL Lacs, the cutoff Lorentz factor ( $\gamma_{\text{cut}}$ ) is  $(1.53 - 25.41) \times 10^4$  which is larger than those typically estimated for EIC-BLR model, as the average energy of the synchrotron photons is lower than that of BLR photons. The highest cutoff Lorentz factor,  $\gamma_{\text{cut}} = (2.54 \pm 0.05) \times 10^5$ , was estimated for SDSS J105707.47+551032.2, which is due to the fact that the synchrotron emission of this source extends up to the X-ray band. The minimum Lorentz factor ranges from 1.08 to 207.0 and is given in

Table 3, constrained by the requirement that the emission at radio bands does not overshoot the observed data.

For the FSRQs the estimated magnetic field ranges between 1.30 and 15.17 G. The highest value,  $15.17 \pm 0.90$  G, was estimated for PMN J0134-3843 which is attributed to the fact that the synchrotron component of this source exhibits a comparable flux compared to its inverse Compton component. Consequently, when the external photons are boosted into the jet frame (with a  $\delta = 24.71$  for this object), their density increases. This requires the presence of lower density electrons, thereby requiring a higher magnetic field to account for the observed synchrotron emission. In contrast to the modeling of FSRQs, when considering BL Lacs, the magnetic field is found to be in the range of 0.001 to 0.04 G. For the FSRQs, except for the bordering cases of PKS B1412-096, PMN J2135-5006, and PMN J1344-1723, where  $\delta$  of 5.24, 5.45, and 47.18 were estimated respectively,  $\delta$  varies within a narrow range of 12.52 to 33.82. This range is typical for blazars. For PMN J1344-1723, a  $\delta$  of 47.18 was estimated due to the pronounced Compton dominance observed in this object. In contrast, a lower  $\delta$  of 5.24 for PKS B1412-096 was estimated because its Compton dominance is nearly 1. Meanwhile,  $\delta = 5.45$  for PMN J2135-5006 was estimated due to its relatively high cutoff Lorentz factor ( $\gamma_{\text{cut}}$ ), which is unconstrained by the data. For the BL Lacs, larger  $\delta$  in the range of 28.94 to 49.84 were estimated. This is because the synchrotron component of these objects peaks around  $10^{13} - 10^{14}$  Hz, so a higher  $\delta$  is required to explain the second peak, which is in the MeV band.

Another key parameter to assess following the modeling is the jet luminosity. The jet power, in the form of electrons and magnetic field, is computed as  $L_e = \pi c R_b^2 \Gamma^2 U_e$  and  $L_B = \pi c R_b^2 \Gamma^2 U_B$ , respectively. Assuming one proton per relativistic emitting electron and that protons are 'cold' in the comoving frame, the total jet luminosity is calculated as  $L_{\text{jet}} = L_e + L_B + L_p$ . The corresponding  $L_e$  and  $L_B$  luminosities are presented in Table 3. For the FSRQs,  $L_e$  varies within the range from  $7.24 \times 10^{43}$  erg s<sup>-1</sup> to  $2.94 \times 10^{45}$  erg s<sup>-1</sup>, while  $L_B$  ranges from  $2.72 \times 10^{42}$  erg s<sup>-1</sup> to  $4.06 \times 10^{45}$  erg s<sup>-1</sup>. Among the considered sources, 33 exhibit an  $L_e/L_B$  ratio in the range of 0.1 to 10, suggesting that the emitting region is close to equipartition. For PKS B1412-096 the ratio  $L_e/L_B = 0.05$  is estimated which is because of the synchrotron component is at the same level as the inverse Compton component. Conversely, for OX 131, 4C +71.07, and PKS 2149-306, a significantly higher ratio with  $L_e/L_B > 100$  is estimated, due to the dominance of the SSC component over the synchrotron component. In the modeling of BL Lacs,  $L_e$  is in the range of  $(0.04 - 3.85) \times 10^{47}$  erg s<sup>-1</sup>, which is higher than the  $L_B$ , ranging from  $(0.10 - 3.92) \times 10^{43}$  erg s<sup>-1</sup>. The relationship between the total jet luminosity ( $L_{\text{jet}}$ ) and redshift is illustrated in Fig. 7 upper panel, where our current source sample (FSRQs in blue and BL Lacs in orange) is compared with sources from Sahakyan et al. (2020) (gray), all of which are FSRQs. Clearly, BL Lacs exhibit different properties and tend to have higher luminosities. However, discussions about the distribution of BL Lacs remain inconclusive. This is because BL Lacs are rarely identified at distances  $z > 2.0$  but a significant fraction of BL Lacs lack robust redshift determination, suggesting that BL Lacs might indeed be present at larger redshifts. In contrast, FSRQs show a similar luminosity range to those at redshifts  $z > 2.5$ . For the FSRQs the highest luminosity of  $6.51 \times 10^{45}$  erg s<sup>-1</sup> was observed for 4C +71.07 at a redshift of  $z = 2.218$ . Upon comparing both samples, it is evident that the jet luminosity tends to increase with source distance, with two notable exceptions: PKS 1351-018 and GB 1508+5714, which have the highest redshifts of  $z = 3.72$  and  $z = 4.31$ , respectively.

The fit presented in Fig. 6 also enables the estimation of disk lumi-



**Figure 7.** *Upper panel:* The dependence of the total jet luminosity ( $L_{\text{jet}}$ ) on redshift. *Middle panel:* The dependence of the disc luminosity ( $L_D$ ) on redshift. *Lower panel:* The correlation between jet luminosity and disc luminosity. The sources from Sahakyan et al. (2020) are shown in gray.

nosity for cases where a thermal blue-bump component is observable. This excess is evident in a total of 37 sources. The disk luminosity,  $L_D$ , varies from  $5.60 \times 10^{44}$  erg s<sup>-1</sup> to  $3.97 \times 10^{47}$  erg s<sup>-1</sup>. The relationship between disk luminosity and redshift for  $\gamma$ -ray blazars with  $z > 2.0$  is depicted in the middle panel of Fig. 7. High disk luminosities of  $1.25 \times 10^{47}$  erg s<sup>-1</sup>,  $2.32 \times 10^{47}$  erg s<sup>-1</sup>,  $3.35 \times 10^{47}$  erg s<sup>-1</sup>, and  $3.97 \times 10^{47}$  erg s<sup>-1</sup> were estimated for PKS 2149-306, 4C +71.07,

2MAS J16561677-3302127, and B2 0552+39A, respectively. Furthermore, the relationship between disk luminosity and jet luminosity is examined in the lower panel of Fig. 7. This relationship can be described by the equation  $\log_{10}(L_{\text{jet}}) = 0.22 \times \log_{10}(L_D) + 34.60$ , represented by the green line in Fig. 7, with the 2 $\sigma$  uncertainty region shown in light green. Notably, sources such as PKS 2149-306 and 4C +71.07 exhibit disk luminosities exceeding  $10^{47}$  erg s<sup>-1</sup> and jet luminosities exceeding  $10^{45}$  erg s<sup>-1</sup>, highlighting their significant energetic output.

## 7 CONCLUSION

High redshift blazars have consistently been the subject of intense investigation due to their crucial role in understanding the connection between jet formation, accretion processes, and black hole development in the early stages of black hole formation. In this paper, we investigate the multiwavelength properties of 79 blazars with redshifts ranging from  $z = 2.0$  to 2.5 using data accumulated by *Fermi*, Swift XRT/UVOT, and NuSTAR.

In the  $\gamma$ -ray band, the flux and photon index of the selected sources span from  $5.32 \times 10^{-10}$  to  $3.40 \times 10^{-7}$  photon cm<sup>-2</sup> s<sup>-1</sup> and between 1.66 and 3.15, respectively, illustrating the diverse characteristics of the sources under consideration. Meanwhile, the luminosity ranges from  $(3.67 \pm 1.37) \times 10^{46}$  to  $(6.62 \pm 0.05) \times 10^{48}$  erg s<sup>-1</sup>, positioning some of these sources among the brightest blazars detected in the  $\gamma$ -ray band. Similarly, in the 0.3-10 keV band, the weakest sources exhibit fluxes on the order of  $(1.06 \pm 0.32) \times 10^{-13}$  erg cm<sup>-2</sup> s<sup>-1</sup>, while the brighter ones reach  $(2.96 \pm 0.02) \times 10^{-11}$  erg cm<sup>-2</sup> s<sup>-1</sup>, with the majority of the sources exhibiting a soft photon index (less than 2.0). This soft photon index extends into the hard X-ray band (3–30 keV), where the index ranges from 1.09 to 1.67. The comparison of  $\gamma$ -ray and X-ray fluxes reveals no clear correlation in time-averaged measurements. This is exemplified by sources such as 4C +71.07 and PKS 2149-306, which are bright in both  $\gamma$ -ray and X-ray bands, and 4C +01.02, which, despite its high  $\gamma$ -ray flux, exhibits only a moderate X-ray flux.

Using the adaptive binning methods for light curve, we found flux variations in 31 sources, with the most pronounced variability in 4C+01.02, 4C+71.07, PKS 0226-559, PKS 1329-049, PKS 2149-306, S3 0458-02, and S4 0917+44. The sources like PKS 2149-306, 4C+71.07, PKS 1329-049 and 4C+01.02 showed significant increases in  $\gamma$ -ray emission, with peak fluxes occasionally exceeding  $10^{-6}$  photon cm<sup>-2</sup> s<sup>-1</sup> while for the other sources show more modest increases in  $\gamma$ -ray flux: the  $\gamma$ -ray fluxes exceed  $10^{-7}$  photon cm<sup>-2</sup> s<sup>-1</sup> during flaring periods. Noticeably, the  $\gamma$ -ray luminosity of 4C+71.07, PKS 1329-049, and 4C+01.02 occasionally was above  $10^{50}$  erg s<sup>-1</sup>, putting them among the most luminous sources in the  $\gamma$ -ray band.

In addition to  $\gamma$ -ray variability, our analysis extended to X-ray and optical/UV bands. Despite the limited data, X-ray flux variability was evident for 4C +71.07, PKS 0226-559, PKS 1329-049, PKS 2149-306, S3 0458-02 and S4 0917+44, while in optical/UV band clear flux variation is found for 4C+01.02, PKS 0226-559 and PKS 2149-306.

In this study, we employed a leptonic one-zone synchrotron and inverse Compton model, considering both internal and external photons, to interpret the multiwavelength SEDs of selected FSRQs and BL Lacs. The range of parameters estimated from the modeling provides a general view of the sources' emissions in an average state. The power-law index of the electrons, indicative of particle acceleration mechanisms, varied from 1.56 to 2.85. For FSRQs the highest energy emissions, as characterized by the cutoff Lorentz factor, varied

**Table 3.** Broadband SED Modeling of the Considered Sources. [1] Source Name. [2] Doppler Factor. [3] Power-Law index of emitting electrons. [4] Minimum Lorentz factor of the electrons and [5] cutoff Lorentz factor in units of 100. [6] Magnetic field, expressed in units of  $G$ . [7] Accretion Disk Luminosity, in units of  $10^{46}$  erg  $s^{-1}$ . [8] and [9] Power of the jet in the form of relativistic electrons ( $L_e$ ) and Magnetic field ( $L_B$ ), both in units of  $10^{44}$  erg  $s^{-1}$ . [10] Luminosity of the jet in the form of protons assuming one proton per relativistic emitting electron in units of  $10^{45}$  erg  $s^{-1}$ .

Source [1]	$\delta$ [2]	$P$ [3]	$\gamma_{\min}$ [4]	$\gamma_{\text{cut}}$ [5]	$B$ [6]	$L_D$ [7]	$L_e$ [8]	$L_B$ [9]	$L_P$ [10]
S5 1053+70	18.42 ± 1.42	2.08 ± 0.21	69.49 ± 7.30	12.50 ± 1.22	3.96 ± 0.42	1.44	4.40	0.76	0.39
PMN J1344-1723	47.18 ± 1.66	2.10 ± 0.06	18.56 ± 1.83	35.32 ± 3.13	4.21 ± 0.27	0.84	2.93	0.08	0.70
PKS 1915-458	24.53 ± 1.14	2.29 ± 0.22	65.94 ± 6.50	4.09 ± 0.69	7.62 ± 0.80	4.14	4.55	0.24	0.62
PKS 0226-559	33.13 ± 2.03	1.56 ± 0.06	17.32 ± 2.23	27.07 ± 2.54	4.25 ± 0.33	7.68	4.37	0.12	0.45
PKS 0601-70	24.91 ± 1.20	1.92 ± 0.17	71.10 ± 6.49	6.39 ± 0.59	5.81 ± 0.62	3.23	3.28	2.43	0.34
B2 1436+37B	21.06 ± 0.96	2.00 ± 0.21	95.07 ± 10.48	4.69 ± 0.42	5.07 ± 0.57	0.75	2.64	1.71	0.25
2MASS J16561677-3302127	17.15 ± 0.22	1.93 ± 0.02	97.22 ± 1.59	14.50 ± 0.29	9.91 ± 0.24	33.50	6.39	2.56	0.42
TXS 1645+635	24.58 ± 0.94	1.92 ± 0.18	67.97 ± 8.10	3.87 ± 0.37	7.46 ± 0.70	1.28	1.70	2.40	0.21
PKS B1149-084	25.62 ± 0.93	1.92 ± 0.19	64.32 ± 6.41	4.86 ± 0.59	5.98 ± 0.39	1.98	1.64	4.50	0.19
S5 0212+73	23.24 ± 0.65	2.66 ± 0.14	207.00 ± 9.11	7.63 ± 0.73	8.48 ± 0.38	9.96	7.23	0.13	0.39
B2 0552+39A	13.93 ± 0.82	2.12 ± 0.07	105.80 ± 7.80	27.18 ± 2.45	6.91 ± 0.77	39.70	5.60	0.43	0.34
PKS 2149-306	25.83 ± 0.83	1.82 ± 0.04	83.20 ± 1.31	3.02 ± 0.12	5.14 ± 0.06	12.50	29.40	0.04	3.16
PKS 1430-178	26.31 ± 1.22	2.25 ± 0.17	43.81 ± 5.82	4.17 ± 0.62	9.80 ± 0.83	6.21	5.32	0.20	1.00
S3 0458-02	33.82 ± 1.37	2.21 ± 0.11	55.51 ± 7.02	7.16 ± 0.75	7.21 ± 0.59	6.08	6.60	1.09	0.93
PMN J0157-4614	22.59 ± 1.43	1.94 ± 0.21	133.10 ± 21.74	4.26 ± 0.68	6.59 ± 0.63	0.69	0.72	2.63	0.05
PKS 0420+022	26.55 ± 1.18	2.78 ± 0.14	48.92 ± 4.10	8.32 ± 0.95	8.01 ± 0.55	3.55	2.31	1.54	0.45
PKS 2245-328	24.98 ± 1.46	1.94 ± 0.23	47.52 ± 6.02	4.15 ± 0.51	8.18 ± 0.74	3.06	2.47	1.86	0.40
PKS B2224+006	21.38 ± 1.01	1.79 ± 0.20	29.27 ± 4.49	3.13 ± 0.38	8.02 ± 0.87	0.25	2.78	1.33	0.59
PKS 2244-37	26.04 ± 1.94	1.99 ± 0.25	63.82 ± 7.72	5.28 ± 0.96	10.89 ± 1.30	4.46	1.59	0.03	0.19
B2 0242+23	26.05 ± 1.26	2.10 ± 0.18	34.78 ± 4.12	4.95 ± 0.69	6.21 ± 0.48	1.93	3.08	0.69	0.62
4C +71.07	32.34 ± 1.30	2.24 ± 0.16	43.72 ± 3.72	4.38 ± 0.40	9.94 ± 0.52	23.20	22.70	0.14	4.23
PKS 2022+031	24.37 ± 1.31	2.18 ± 0.17	32.99 ± 3.38	11.10 ± 1.17	7.10 ± 0.84	0.12	2.32	0.96	0.45
MG2 J153938+2744	19.46 ± 0.80	2.12 ± 0.13	51.00 ± 3.55	8.96 ± 0.96	8.28 ± 0.52	0.30	1.50	8.67	0.20
S4 0917+44	27.14 ± 0.81	2.42 ± 0.11	69.94 ± 6.35	8.84 ± 0.67	5.32 ± 0.26	3.83	7.48	1.27	0.91
PMN J2135-5006	5.45 ± 0.21	2.85 ± 0.06	158.70 ± 14.13	355.10 ± 48.94	1.30 ± 0.10	0.66	3.23	2.85	0.18
OX 131	21.83 ± 0.77	1.60 ± 0.12	109.00 ± 10.71	13.76 ± 0.93	1.76 ± 0.10	0.41	4.30	0.04	0.21
PMN J1959-4246	20.98 ± 0.84	2.02 ± 0.17	57.41 ± 4.50	5.07 ± 0.63	7.88 ± 0.71	0.17	2.54	1.13	0.34
PKS 0446+11	23.19 ± 1.12	1.98 ± 0.17	16.67 ± 2.26	5.53 ± 0.73	5.34 ± 0.46	0.16	4.36	8.05	1.42
PKS 1329-049	22.29 ± 0.87	2.30 ± 0.16	69.16 ± 8.12	12.00 ± 1.99	3.62 ± 0.34	6.52	8.00	0.43	0.87
PMN J0134-3843	24.71 ± 0.98	2.54 ± 0.19	86.57 ± 8.43	4.61 ± 0.61	15.17 ± 0.90	9.01	1.59	1.40	0.19
87GB 080551.6+535010	26.16 ± 1.11	1.90 ± 0.20	59.01 ± 5.16	3.34 ± 0.34	4.58 ± 0.40	3.78	3.21	0.46	0.46
PKS B1043-291	26.98 ± 1.61	2.50 ± 0.20	56.45 ± 4.78	10.30 ± 1.28	9.58 ± 1.15	1.89	1.80	0.88	0.25
OM 127	22.03 ± 1.16	2.59 ± 0.14	49.91 ± 5.54	18.73 ± 3.19	7.31 ± 0.66	2.48	2.56	1.90	0.42
PKS 0227-369	20.02 ± 0.68	2.83 ± 0.09	81.14 ± 8.13	25.89 ± 2.97	5.32 ± 0.50	2.52	3.59	1.22	0.41
OF 200	15.55 ± 0.59	2.13 ± 0.11	38.66 ± 1.92	11.03 ± 0.68	5.45 ± 0.24	1.22	2.14	0.88	0.35
B3 0803+452	19.64 ± 0.94	2.28 ± 0.25	44.72 ± 5.38	3.17 ± 0.43	8.56 ± 0.77	1.35	2.11	3.03	0.42
4C +01.02	26.29 ± 0.98	1.88 ± 0.13	28.05 ± 2.99	5.55 ± 0.52	3.04 ± 0.19	2.08	9.23	5.25	1.88
PKS 1348+007	24.93 ± 1.94	1.70 ± 0.21	59.32 ± 8.57	7.87 ± 0.81	2.50 ± 0.29	0.04	2.95	2.19	0.27
SDSS J100326.63+020455.6	26.93 ± 0.76	2.03 ± 0.08	40.09 ± 1.28	7.69 ± 0.39	12.03 ± 0.28	1.12	1.75	0.13	0.27
PKS 0528+134	15.71 ± 0.87	2.15 ± 0.10	46.04 ± 5.30	20.93 ± 2.60	3.67 ± 0.25	0.80	7.91	0.90	1.01
TXS 0322+222	31.80 ± 0.99	2.12 ± 0.25	122.40 ± 11.04	2.38 ± 0.22	7.92 ± 0.58	4.45	3.51	0.51	0.32
4C +13.14	20.30 ± 1.03	1.72 ± 0.14	44.37 ± 5.16	4.10 ± 0.43	8.13 ± 0.62	11.00	3.38	1.21	0.49
PMN J0625-5438	12.52 ± 0.70	2.61 ± 0.23	200.50 ± 27.17	13.10 ± 2.07	5.12 ± 0.55	3.38	2.38	0.95	0.12
OX 110	24.62 ± 0.87	2.08 ± 0.08	29.37 ± 2.40	18.94 ± 1.26	4.89 ± 0.23	0.86	1.06	0.29	0.19
PKS 0549-575	27.49 ± 2.14	1.86 ± 0.21	37.63 ± 4.32	4.47 ± 0.43	6.42 ± 0.69	0.06	3.22	1.29	0.52
PKS B1412-096	5.24 ± 0.17	2.32 ± 0.14	199.30 ± 17.68	13.22 ± 1.08	3.17 ± 0.26	2.17	2.20	40.60	0.10
SDSS J145059.99+520111.7	40.41 ± 0.35	1.71 ± 0.01	1.41 ± 0.03	153.30 ± 1.30	$(1.08 \pm 0.01) \times 10^{-2}$	–	245.50	0.26	105.50
PMN J0124-0624	49.66 ± 0.67	2.09 ± 0.01	2.67 ± 0.07	378.70 ± 10.95	$(1.91 \pm 0.06) \times 10^{-3}$	–	1126.00	0.22	1196.00
SDSS J105707.47+551032.2	28.94 ± 0.43	2.15 ± 0.01	1.08 ± 0.03	2541.00 ± 47.98	$(1.72 \pm 0.02) \times 10^{-2}$	–	59.21	1.53	159.80
1RXS J032342.6-011131	29.71 ± 0.19	1.90 ± 0.004	1.84 ± 0.01	439.90 ± 5.40	$(3.99 \pm 0.04) \times 10^{-2}$	–	40.14	3.92	27.82
NVSS J090226+205045	49.84 ± 0.33	1.79 ± 0.01	22.93 ± 0.23	212.60 ± 2.17	$(4.36 \pm 0.04) \times 10^{-3}$	–	514.00	1.14	38.29
87GB 105148.6+222705	29.10 ± 0.67	2.13 ± 0.01	2.37 ± 0.10	363.80 ± 10.50	$(7.32 \pm 0.22) \times 10^{-3}$	–	936.70	0.93	1235.00
PKS 0437-454	44.39 ± 1.43	1.94 ± 0.01	1.34 ± 0.06	171.20 ± 5.92	$(1.65 \pm 0.07) \times 10^{-3}$	–	3852.00	0.10	4502.00

broadly from  $237.6$  to  $3.53 \times 10^3$ , reflecting the diverse characteristics of the sources studied. The total jet luminosity varied within a relatively narrow range from  $3.20 \times 10^{44}$  to  $6.51 \times 10^{45}$  erg  $s^{-1}$ . The disk luminosity, estimated for sources with discernible thermal components in their SEDs, provided insights into the accretion processes. These disk luminosities, ranging dramatically from  $4.15 \times 10^{44}$  to  $3.97 \times 10^{47}$  erg  $s^{-1}$ , highlighted the varying scales of accretion efficiency and energy conversion in these sources.

In summary, this comprehensive study of 79 high-redshift blazars illuminates the intricate dynamics and energetic processes at play

in these distant and powerful objects. Our findings, encompassing a broad spectrum of multiwavelength observations, highlight the diverse characteristics and behaviors of blazars, underscoring their value in probing the physics of jet formation and accretion processes, and black hole development in the early Universe. The observed variations in flux and luminosity across different bands provide key insights into the particle acceleration and emission mechanisms. Future investigations, when a larger number of distant blazars are known, will allow a more systematic and statistical comparison of their emission properties, thereby unveiling the complexities of these energetic

sources and providing a window into the HE universe and its evolution over cosmic time.

## ACKNOWLEDGEMENTS

We acknowledge the use of analysis tools and services from the Markarian Multiwavelength Data Center (<https://mmdc.am>), the Astrophysics Science Archive Research Center (HEASARC) platforms, as well as data from the Fermi-LAT, Swift and NuSTAR telescopes. This work was supported by the Higher Education and Science Committee of the Republic of Armenia, in the frames of the research project No 21T-1C260.

## DATA AVAILABILITY

The data underlying this article will be shared on reasonable request to the corresponding author.

## REFERENCES

- Abdo A. A., et al., 2010, *ApJ*, **716**, 30
- Abdollahi S., et al., 2022, *ApJS*, **260**, 53
- Ackermann M., et al., 2017, *ApJ*, **837**, L5
- Ajello M., et al., 2022, *ApJS*, **263**, 24
- Ansoldi S., et al., 2018, *ApJ*, **863**, L10
- Arnaud K. A., 1996, in Jacoby G. H., Barnes J., eds, *Astronomical Society of the Pacific Conference Series Vol. 101, Astronomical Data Analysis Software and Systems V*. p. 17
- Arsioli B., Chang Y. L., 2018, *A&A*, **616**, A63
- Atwood W. B., et al., 2009, *ApJ*, **697**, 1071
- Baghmanyan V., Gasparyan S., Sahakyan N., 2017, *ApJ*, **848**, 111
- Bégué D., Sahakyan N., Dereli Bégué H., Giommi P., Gasparyan S., Khachatryan M., Casotto A., Pe’er A., 2023, *arXiv e-prints*, p. [arXiv:2311.02979](https://arxiv.org/abs/2311.02979)
- Blandford R. D., Znajek R. L., 1977, *MNRAS*, **179**, 433
- Błażejowski M., Sikora M., Moderski R., Madejski G. M., 2000, *ApJ*, **545**, 107
- Bloom S. D., Marscher A. P., 1996, *ApJ*, **461**, 657
- Böttcher M., Reimer A., Sweeney K., Prakash A., 2013, *ApJ*, **768**, 54
- Britto R. J., Bottacini E., Lott B., Razzaque S., Buson S., 2016, *ApJ*, **830**, 162
- Cash W., 1979, *ApJ*, **228**, 939
- Cerruti M., Zech A., Boisson C., Emery G., Inoue S., Lenain J.-P., 2019, *MNRAS*, **483**, L12
- Chang Y. L., Brandt C. H., Giommi P., 2020, *Astronomy and Computing*, **30**, 100350
- D’Ammando F., Orienti M., 2016, *MNRAS*, **455**, 1881
- Dermer C. D., Schlickeiser R., 1994, *ApJS*, **90**, 945
- Dermer C. D., Schlickeiser R., Mastichiadis A., 1992, *A&A*, **256**, L27
- Evans P. A., et al., 2009, *MNRAS*, **397**, 1177
- Franceschini A., Rodighiero G., Vaccari M., 2008, *A&A*, **487**, 837
- Gao S., Fedynitch A., Winter W., Pohl M., 2019, *Nature Astronomy*, **3**, 88
- Gasparyan S., Sahakyan N., Baghmanyan V., Zargaryan D., 2018, *ApJ*, **863**, 114
- Gasparyan S., Bégué D., Sahakyan N., 2022, *MNRAS*, **509**, 2102
- Ghisellini G., Tavecchio F., 2015, *MNRAS*, **448**, 1060
- Ghisellini G., Maraschi L., Treves A., 1985, *A&A*, **146**, 204
- Ghisellini G., et al., 2010, *MNRAS*, **405**, 387
- Ghisellini G., et al., 2011, *MNRAS*, **411**, 901
- Giommi P., et al., 2021, *MNRAS*, **507**, 5690
- Harrison F. A., et al., 2013, *ApJ*, **770**, 103
- IceCube Collaboration et al., 2018a, *Science*, **361**, 147
- IceCube Collaboration et al., 2018b, *Science*, **361**, eaat1378
- Keivani A., et al., 2018, *ApJ*, **864**, 84
- Li S., Sun L.-M., Liao N.-H., Fan Y.-Z., 2020, *ApJ*, **900**, 72
- Liao N.-H., Dou L.-M., Jiang N., Wang Y.-B., Fan Y.-Z., Wang T.-G., 2019, *ApJ*, **879**, L9
- Lott B., Escande L., Larsson S., Ballet J., 2012, *A&A*, **544**, A6
- Mannheim K., 1993, *A&A*, **269**, 67
- Mannheim K., Biermann P. L., 1989, *A&A*, **221**, 211
- Maraschi L., Ghisellini G., Celotti A., 1992, *ApJ*, **397**, L5
- Marcotulli L., et al., 2017, *ApJ*, **839**, 96
- Massaro E., Tramacere A., Perri M., Giommi P., Tosti G., 2006, *A&A*, **448**, 861
- Middei R., Giommi P., Perri M., Turriziani S., Sahakyan N., Chang Y. L., Leto C., Verrecchia F., 2022, *MNRAS*, **514**, 3179
- Mücke A., Protheroe R. J., 2001, *Astroparticle Physics*, **15**, 121
- Mücke A., Protheroe R. J., Engel R., Rachen J. P., Stanev T., 2003, *Astroparticle Physics*, **18**, 593
- Murase K., Oikonomou F., Petropoulou M., 2018, *ApJ*, **865**, 124
- Orienti M., D’Ammando F., Giroletti M., Finke J., Dallacasa D., 2016, *Galaxies*, **4**, 26
- Pacciani L., et al., 2012, *MNRAS*, **425**, 2015
- Padovani P., Giommi P., 1995, *ApJ*, **444**, 567
- Padovani P., et al., 2017, *A&ARv*, **25**, 2
- Padovani P., Giommi P., Resconi E., Glauch T., Arsioli B., Sahakyan N., Huber M., 2018, *MNRAS*, **480**, 192
- Paliya V. S., 2015, *ApJ*, **804**, 74
- Paliya V. S., et al., 2015, *ApJ*, **803**, 112
- Paliya V. S., Parker M. L., Fabian A. C., Stalin C. S., 2016, *ApJ*, **825**, 74
- Paliya V. S., Marcotulli L., Ajello M., Joshi M., Sahayanathan S., Rao A. R., Hartmann D., 2017, *ApJ*, **851**, 33
- Paliya V. S., et al., 2019, *ApJ*, **871**, 211
- Petropoulou M., Mastichiadis A., 2015, *MNRAS*, **447**, 36
- Rani B., Lott B., Krichbaum T. P., Fuhrmann L., Zensus J. A., 2013, *A&A*, **557**, A71
- Righi C., Tavecchio F., Pacciani L., 2019, *MNRAS*, **484**, 2067
- Sahakyan N., 2018, *ApJ*, **866**, 109
- Sahakyan N., 2019, *A&A*, **622**, A144
- Sahakyan N., 2021, *MNRAS*, **504**, 5074
- Sahakyan N., Gasparyan S., 2017, *MNRAS*, **470**, 2861
- Sahakyan N., Giommi P., 2022, *MNRAS*, **513**, 4645
- Sahakyan N., Baghmanyan V., Zargaryan D., 2018, *A&A*, **614**, A6
- Sahakyan N., Israyelyan D., Harutyunyan G., Khachatryan M., Gasparyan S., 2020, *MNRAS*, **498**, 2594
- Sahakyan N., Vardanyan V., Khachatryan M., 2022a, *MNRAS*,
- Sahakyan N., Israyelyan D., Harutyunyan G., Gasparyan S., Vardanyan V., Khachatryan M., 2022b, *MNRAS*, **517**, 2757
- Sahakyan N., Giommi P., Padovani P., Petropoulou M., Bégué D., Boccardi B., Gasparyan S., 2023a, *MNRAS*, **519**, 1396
- Sahakyan N., Harutyunyan G., Israyelyan D., 2023b, *MNRAS*, **521**, 1013
- Sikora M., Begelman M. C., Rees M. J., 1994, *ApJ*, **421**, 153
- Tramacere A., 2020, *JetSet: Numerical modeling and SED fitting tool for relativistic jets* (ascl:2009.001)
- Tramacere A., Giommi P., Perri M., Verrecchia F., Tosti G., 2009, *A&A*, **501**, 879
- Tramacere A., Massaro E., Taylor A. M., 2011, *ApJ*, **739**, 66
- Urry C. M., Padovani P., 1995, *PASP*, **107**, 803
- Wood M., Caputo R., Charles E., Di Mauro M., Magill J., Perkins J. S., Fermi-LAT Collaboration 2017, in *35th International Cosmic Ray Conference (ICRC2017)*. p. 824 ([arXiv:1707.09551](https://arxiv.org/abs/1707.09551)), doi:10.22323/1.301.0824
- Zargaryan D., Gasparyan S., Baghmanyan V., Sahakyan N., 2017, *A&A*, **608**, A37

This paper has been typeset from a  $\text{\TeX}/\text{\LaTeX}$  file prepared by the author.